UNIVERSITY OF CALIFORNIA
RIVERSIDE

The Direct Tunneling, Dielectric Breakdown Investigation, and RRAM Application in MBE Hexagonal Boron Nitride Monolayers Using Metal-Insulator-Metal Devices

A Thesis submitted in partial satisfaction
of the requirements for the degree of

Master of Science

in

Electrical Engineering

by

Zhenjun Cui

December 2019

Thesis Committee:
Dr. Jianlin Liu, Chairperson
Dr. Ming Liu
Dr. Yongtao Cui

The Thesis of Zhenjun Cui is approved:

Committee Chairperson

University of California, Riverside

ACKNOWLEDGEMENTS

First of all, I would like to express the deepest appreciation to my advisor, Prof. Jianlin Liu, who gave me the precious research opportunities and valuable guidance on both study and life in the past three years. The scientific thinking strategy and the spirit of hardworking and team-work learned from Dr. Liu will definitely benefit me forever. Apart from my advisor, I would like to thank Dr. Yongtao Cui and Dr. Ming Liu, who are my master final dissertation defense as well as my previous Ph.D. oral qualifying committee members, for providing insightful comments and helpful advice.

With a special mention to my friends and fellow lab mates in the Quantum Structures Laboratory: Dr. Renjing Zheng, Dr. Alireza Khanaki, Dr. Mohammad Suja, Dr. Sunayna Bashar, Dr. Zheng Zuo, Dr. Zhongguang Xu, Dr. Long Xu, Dr. Caixia Xu, Mr. Hao Tian, Mr. Yanwei He, Mr. Ivan Jiang and Mr. Wenhao Shi who consistently supported and helped me during the three-year studies. It was fantastic to work with every one of you. I am also grateful to all my dear friends I met in UCR. As a person who can't drive in California, I literally can't live without my friends. All the good days we spent together will be deeply memorized and our friendship will definitely last forever.

Finally, I would like to thank my family for their unconditional love and supports.

ABSTRACT OF THE THESIS

The Direct Tunneling, Dielectric Breakdown Investigation, and RRAM Application in MBE Hexagonal Boron Nitride Monolayers Using Metal-Insulator-Metal Devices

by

Zhenjun Cui

Master of Science, Graduate Program in Electrical Engineering
University of California, Riverside, December 2019
Dr. Jianlin Liu, Chairperson

In today's post-Moore era, low-dimensional materials and their potential electronic applications have attracted extensive attention, but high-quality material synthesis and complicated device physics investigation remains challenging. Our lab is able to use Molecular Beam Epitaxy (MBE) to reliably grow high quality millimeter grain size continuous ultrathin two-dimensional(2D) hexagonal boron-nitridefilm (h-BN) on Cobalt (Co) and Nickle (Ni) catalytic transition metal substrates. This is highly advantageous in 2D electronic and photonic device applications. In this thesis, we report our comprehensive electrical tunneling, dielectric breakdown, and memory application of single-layer h-BN film by fabricating scablable Metal-insulator-metal (MIM) diodes.

Direct tunneling and dielectric breakdown in molecular beam epitaxial hexagonal boron nitride (h-BN) monolayers were studied based on Ni/h-BN/Ni device configuration in Chapter 2. Effective tunneling areas are orders of magnitude smaller than the physical areas of the devices. Statistical Weibull analysis of the breakdown characteristics shows that breakdown area-scaling law applies to the effective areas rather than physical areas of the devices. The h-BN based MIM devices can sustain repeated DC voltage sweeping

stresses up to 85 times under an extremely high compliance current of 100 mA, and the critical electric field is determined to be at least 11.8 MV/cm, demonstrating high dielectric strength and reliability of these h-BN monolayers. The mechanism of the breakdown and recovery of the h-BN monolayer MIM devices is also discussed.

The second project (Chapter 3) is devoted to the evaluation of Resistive Random Access Memory (RRAM) devices and the mechanism discussion of monolayer h-BN in MIM structure. The memory performance of bipolar switching shows great endurance with 97 cycles at 100mA compliance current, and a high average 10^3 on/off ratio, but the reliability is an issue. For this particular film, both non-volatile bipolar and unipolar resistive switching (RS) and volatile threshold (TH) switching phenomena were found to coexist and could be converted from one to the other by controlling the electrical power, which provides a better understanding of the switching models. In devices with graphene bottom electrodes, bipolar resistive switching with self compliance current is discovered, making h-BN a potential candidate in low-power device applications.

Table of Contents

List of Figures

Figure 2.9 (a)I-V curves of 97 devices with an area of 25 × 25 μm^2. (b) I-V curves of 96 devices with an area of 50 × 50 μm^2. (c) I-V curves of 30 devices with an area of 100 × 100 μm^2. (d) I-V curves of 50 devices with an area of 200 × 200 μm^2. (e) Schematic of direct tunneling mechanism of Ni/h-BN/Ni device.(f) The cumulative probability distribution of $I_{tunneling}$ with different device areas. All tunneling currents were collected at a bias of 0.1 V. Black, red, magenta and blue symbols represent devices with size 25×25, 50×50, 100×100 and 200×200 μm^2, respectively. The inset is the peak tunneling current ($\mathbf{I}_{\boldsymbol{peak}}$) as a function of device area, where $\mathbf{I}_{\boldsymbol{peak}}$ is the 63% of cumulative current value. Tunneling current being not linearly proportional to device area is evident.

Figure 2.10 (a) Histogram of breakdown voltage distribution with a bin size of 0.1 V and relevant Gaussian distribution fittings. (b) Cumulative failure probability F as a function of V_{BD}. (c) Weibull plot of breakdown voltage distribution. (d) Normalized Weibull plot by scaling effective areas A_{eff} to 1 μm^2. Data overlapping for $A1_{eff}$-$A3_{eff}$ in most of breakdown voltage ranges and $A4_{eff}$ at higher voltage range is acceptable.

Figure 3.1 Characterization of 2D h-BN layer (Sample 2). (a) SEM image of h-BN film on Ni substrate. (b) Raman spectrum measured on the transferred h-BN on SiO_2/Si. (c) UV absorption spectrum of h-BN transferred onto a sapphire substrate. Inset shows the Tauc plot determining the optical bandgap. (d) AFM image scanning across the sample edge on the transferred h-BN on SiO_2/Si.

Figure 3.2 Characterization of h-BN/Gr sample (Sample 3). (a) SEM image of continuous h-BN/Gr film on Co substrate. (b)Raman spectrum measured directly on the h-BN/Gr on Co. (c) UV absorption spectrum of h-BN transferred onto a sapphire substrate. Inset shows the Tauc plot determining the optical bandgap. (d) AFM image of the same sample transferred onto SiO_2/Si substrate with the total thickness of ~133 nm. (e) C1s and (f) B1s and N1s as a function of sputtering depth in the depth-profile XPS characterization.

Figure 3.3 I-V characteristics on three distinct Au-h-BN-Ni devices showing forming free (a) non-volatile bipolar resistive switching (BRS) mode, (b) non-volatile unipolar resistive switching (URS) mode, and (c) volatile threshold (TH) switching mode. The compliance current is 100mA.

Figure 3.4 BRS performance on an Au-h-BN-Ni device with size 50x50 μm^2 from Sample 2. (a) I-V characteristics of successive 97 BRS cycles; (b) Time dependent current measurements featuring stable LRS but unsatisfied HRS retention at room temperature. The current of the HRS and LRS is measured at the bias of 0.1 V; (c) The dispersion of both HRS and LRS in terms of the current read at 0.1V with the 97 cycles; (d) The cumulative set and reset voltage distribution.

Figure 3.5 I-V characteristics in sequence on one Pt-h-BN-Ni device, (a)-(c) shows the conversion from BRS to TH switching, and URS with respect to the increase of the set voltage.

Figure 3.6 I-V characteristics in sequence on one Au-h-BN-Graphite-Co device, (a)-(d) shows the conversion from BRS with self-compliance current to URS, and resets back to BRS, and move on to URS behavior in sequence. Conversion of BRS and URS is controlled by compliance current value.

Figure 3.7 RS Phenomena summary on monolayer h-BN film with various electrodes. (a)-(c) are collected from Ni-h-BN-Ni, (a)-(b) BRS conversion to URS on one device, (c) individual TH behavior; (d)-(f) show independent BRS, URS and TH events on are on Pt-h-BN-Ni.(g)-(i) are collected on Co-h-BN-Gr-Co; (g) and (h) demonstrate the transition from BRS with self-compliant current to URS; (i) is an example of independent TH characteristics; (j)-(l) show the independent BRS, URS and TH behaviors on Au-h-BN-Gr-Co with a cc 100 mA.

Figure 3.8 Schematic diagram of the resistive switching mechanisms of Metal-h-BN-Ni devices. The top electrodes in our experiments include Ni, Au and Pt. (a) Pristine state. Silver, dark blue and light blue areas represent the electrodes, h-BN and interfaces, respectively. Hollow circles are non-conductive defects. The percolating path denoted by a solid black path in (b) and (d) connecting the two terminal electrodes through monolayer h-BN and the interface between h-BN and electrodes. The initial developed conduction filaments are normally very stable like (b) shows, and the LRS of BRS operation can be achieved with respect of bias. By applying the opposite voltage, the CF ruptures so that the devices are able to recover to the HRS shown in (c). If the CF are less stable compared to (b), as shown in (d), which is either formed from the initial state or followed BRS events by increasing the electric power. Then, Joule heat dominates the driving force of the resistive switching, indicating the reversible URS or TH mode can be obtained depending on the following external bias sweep direction.

Figure 3.9 Schematic diagram of the resistive switching mechanisms of Metal-h-BN-Gr-Co devices, Au and Co are used as top electrodes. Silver, dark blue, light blue and brown areas represent the electrodes, h-BN, interfaces and Graphite, respectively. Hollow circles and solid dots are non-conductive and conductive defects, respectively. (a) Original state. (b) When an incomplete CF is formed as shown in (b), the LRS of self compliance current limited BRS is initialized. The current limiter is most probably emerged in the interface between h-BN and Graphite. The break of the incomplete CF turns the device back to HRS like (c) shows. If the electric power is enhanced after (c) or large enough initially after (a), then the complete CF between the two electrodes is able to developed. And BRS, URS and TH with compliance current can be achieved depending on the polarity and direction of the later bias.

List of Tables

Chapter 1 Introduction and experiment description

1.1 Hexagonal boron nitride (h-BN)

Hexagonal boron nitride (h-BN), known as "white Graphene", is an important member of the Graphene based 2D crystal material family. h-BN refers to layered nanomaterial with a honeycomb lattice structure composed by boron (B) and nitrogen (N) atoms with strong covalent bond in-plane and weak van der Waals (vdW) force between layers (Figure 1.1), just like Graphene [1].

H-BN is regarded as a semiconductor thanks to the wide band gap (~ 5.9 eV) [2], as well as an excellent 2D dielectric due to the excellent dielectric property (relative permittivity ~4) [3], which is comparable with SiO_2 (~3.9) [4]. H-BN also shows extraordinary thermal and chemical stability, which allows h-BN based devices work under extreme conditions [5]. So far, h-BN is widely used as the gate barrier and substrate of other vdW material electronic devices, especially graphene [6], because of its atomically ultra-flat surface (root mean square (RMS) roughness < 0.2), free of dangling bonds [7] and extremely small in-plane lattice mismatch with graphene (~1.7%) [8]. These remarkable properties define 2D h-BN as an ideal dielectric material to gate, encapsulate, or insulate other 2D materials towards novel nanoelectronic devices that possess unparalleled high performance over state of the art counterparts based on three-dimensional materials. Furthermore, several studies of the electrical tunneling, [9][10] oxidation resistance [11], mechanical [12], optical [13], phonon [14], hydrophobic [15] and piezoelectric [16] properties of BN have also been reported. These properties make h-BN an ideal functional material for a wide range of novel applications, such as ultraviolet (UV) light-emitting devices [17], power electronics [18], nonvolatile memories [19], electronic

packaging [20], fuel cells [21], and biomedicine [22], etc.

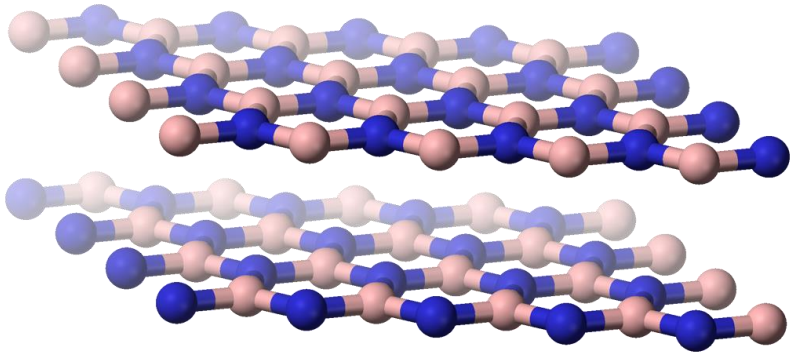

Figure 1.1 Idealized structure of hexagonal boron nitride (h-BN) sheets. Blue and pink atoms are representative of boron and nitrogen atoms (adapted from Wikipedia)

1.2 H-BN synthesis methods

The first step of investigation is to obtain 2D h-BN single layer and few layers. To date, it is still challenging to produce a large yield of high quality, large lateral scale and thickness controllable 2D h-BN nanosheets or get desired structure or to the properties for specific functions.

Like most 2D vdW material fabrication strategies, the most common h-BN synthesis approaches include, but are not limited to, mechanical exfoliation [23], liquid exfoliation [24], epitaxy techniques like chemical vapor deposition (CVD) [25], molecular beam epitaxy (MBE) [26] and several other new fabrication methods [27-32].

Among all the techniques, the exfoliation process is most feasible at a low cost, which motivates and accelerates the development of 2D materials. But the h-BN achieved by this method is generally in flakes, whose size or layer number are uncontrollable. Additionally, this method produces a limited quantity film, which is randomly distributed and may contain chemical contaminations. Compared with exfoliation, epitaxy

techniques can grow large scale continuous h-BN film with controllable number of layers, which has better quality.

In Quantum Structures Lab (QSL), we use Perkin Elmer 425 Molecular Beam Epitaxy (MBE) system (Figure 1.2) to grow h-BN, other 2D vdW materials and heterostructures [33-38]. MBE is a technique to obtain high-quality crystalline epitaxial thin films in an ultrahigh vacuum (UHV) environment. It has evident advantage over other synthesis methods in terms of more precise control of thickness, composition and morphology.

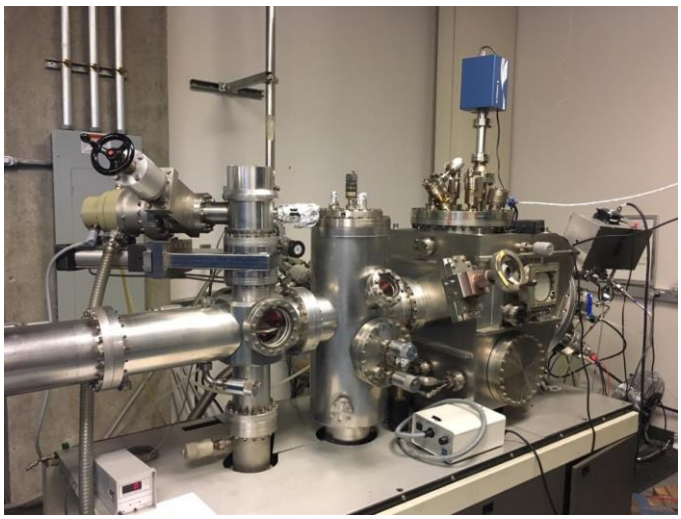

Figure 1.2 A modified 425B Perkin Elmer MBE system in Quantum Structures Laboratory (QSL) at University of California, Riverside (UCR).

1.3 Experimental description

The second step is to fabricate a suitable device based on these 2D h-BN layers. Towards the study of electrical and dielectric properties and applications, a straightforward type: metal-insulator-metal (MIM) configuration is applied. The experiment procedures performed in Chapter 2 and Chapter 3 are almost identical, which are demonstrated as follows, including the h-BN sample synthesis and characterization as

well as the MIM device fabrication and measurement.

1.3.1 H-BN sample synthesis

Substrate Preparation: Commercial Ni foil (0.1 mm thick and 99.995% purity) used in Chapter 2 and 3 and Co foil (0.1 mm thick, 99.95% purity) used in Chapter 3 from Alfa Aesar were the substrates. As-received foils were polished by an SBT 920 Lapping and Polishing workstation. Then, they were cut into 1 cm × 1 cm pieces as substrates, degreased with acetone and IPA, etched by diluted HCl solution (10%) for 2 min to remove the native oxides, and rinsed with deionized water. After blown-dry using a nitrogen gun, the fresh substrates were immediately loaded onto substrate holders and transferred to the growth chamber.

Hydrogen Annealing and Carburization: A plasma-assisted Perkin-Elmer MBE system with a background pressure of ~10^{-9} Torr was used for the sample growth. The substrate was heated to around 950 °C and annealed at this temperature under a 10 sccm flow of hydrogen gas for 10 to 60 mins. Then, the substrate temperature was adjusted to the growth temperature. 0.5 sccm Acetylene gas (C_2H_2, Airgas, 99.999% purity) was introduced into chamber to enrich substrate with carbon prior to h-BN growth. H-BN growth step started after the carburization process.

H-BN Growth: A Knudsen effusion cell filled with B_2O_3 powder (Alfa Aesar, 99.999% purity) was used as boron (B) source. Nitrogen plasma (Airgas, 99.9999% purity) generated by an electron cyclotron resonance (ECR) system and high-purity ammonia (American Gas Group, 99.9995% purity) were used as nitrogen (N) sources. The h-BN growth was conducted by simultaneous introduction of B and N sources onto the substrate at 900–930 °C and lasts 6 hrs to 8hrs. B cell temperature was maintained at constant temperature throughout

the growth, which is around 1150 °C (1120-1170°C). NH_3 gas was controlled at a constant flow rate which is limited up to 10 sccm by a mass flow controller (MFC) and introduced to the chamber through a shut-off valve. Total gas flow rate is limited up to 15 sccm by the turbo pump ability. Nitrogen plasma as an alternative N source is generated from an ECR plasma source with a power of 228 W. After the growth, the samples were cooled to room temperature, all the substrate heating/cooling rate was ~10 °C min^{-1}. The detailed growth conditions of the samples used in Chapter 2 and 3 are summarized in Table 2.1 and Table 3.1, respectively. We synthesized 5 h-BN samples in total, four of the five are h-BN directly grown on metal substrate, except the Sample 3 of Chapter 3, which is h-BN/Graphite grown on Co foil.

Transferring of h-BN Samples: As-grown samples were spin-coated first with PMMA (495 A4). Then, the samples were put into $FeCl_3$/HCl solution for approximately a day to etch the Ni foil or the Co foil substrate. Thereafter, the stacked PMMA/h-BN stack or PMMA/h-BN/G was transferred into 10% HCl, 5% HCl and DI water successively to rinse out the residual etchant. Then, the floating PMMA/h-BN or PMMA/h-BN/G was taken out by desired substrates (SiO_2/Si or sapphire) and left to dry in air for at least 12 hours. After that, a few drops of PMMA were deposited again on the transferred film and soaked for another two hours. These additional drops of PMMA soften the previous PMMA layer and enhance the attachment of h-BN or h-BN/G on the substrate. PMMA was removed by dipping the sample into acetone bath. In the last step, the h-BN/G sample was dried at 40 °C on a hot plate for a couple of hours without annealing. While, the other h-BN samples were annealed at 400 °C inside a CVD furnace for 3 hrs in Ar/O_2 flow of 300 sccm to remove any remaining organic residue.

1.3.2 H-BN sample characterization

Scanning electron microscopy (SEM) images were acquired using an FEI NNS450 SEM system in secondary electron mode (SE) imaging mode with a beam voltage of 10 kV. Raman characterizations were performed using a HORIBA LabRam system equipped with a 60 mW, 532 nm green laser. A Varian Cary 500 double-beam scanning ultraviolet/visible/near-infrared (UV/vis/NIR) spectrophotometer was used for absorption measurements. X-ray photoelectron spectroscopy (XPS) characterization was conducted using a Kratos AXIS ULTRA XPS system equipped with an Al Kα monochromatic x-ray source and a 165 mm mean radius electron energy hemispherical analyzer. The depth-profile XPS characterization was performed on a 3×3 mm^2 area of the sample using a 2 keV Ar ion beam sputter with an etching rate of 1 nm min^{-1}. The fitting of XPS data was performed using CasaXPS software. As-measured XPS data were first calibrated by using Ni 2p3/2 peak at 852.6 eV or Co 2p3/2 peak at 778.1 eV (Lorentzian Asymmetric line shape). B 1s, N 1s and C 1s peaks were convoluted with Gaussian/Lorentzian line shape after background-corrected by Shirley type background. Atomic force microscopy (AFM) images were obtained using a Veeco D5000 AFM system.

1.3.3 Device fabrication and electrical measurement

Two terminal MIM diodes based on h-BN /Ni or h-BN /G/ Co sample were fabricated by a standard photolithography and lift-off processes. The metallic substrate acted as bottom electrode, which strongly simplifies the fabrication process. The 50nm-100nm metal contact layer including active top contacts like Nickle (Ni), Cobalt (Co), or inert electrodes such as Gold (Au), Platinum (Pt) was deposited by e-beam evaporation or sputtering as top square contacts with an edge length of 25μm, 50 μm,200μm, and 400μm on

the surface of the as-grown h-BN film, which denoted as A1, A2, A3 and A4, respectively. Ni was the one and only top electrode used in Chapter 2, and all the other metals were deposited for the study of Chapter 3. Reactive ion etching (RIE) was performed with a 50 sccm SF_6 plasma, under a power of 600 W, and for 15 s to etch the h-BN film between devices, which ensured isolation of different devices on the same substrate. Agilent 4155C semiconductor parameter analyzer equipped with probing tips of about 5 μm and sample stage (Signatone, SE-TL) was used to measure the electric property of MIM devices.

1.4 Reference

[1] Nag, Angshuman, et al. "Graphene analogues of BN: novel synthesis and properties." *ACS nano* 4.3 (2010): 1539-1544.

[2] Cassabois, Guillaume, Pierre Valvin, and Bernard Gil. "Hexagonal boron nitride is an indirect bandgap semiconductor." *Nature Photonics* 10.4 (2016): 262.

[3] Kim, Ki Kang, et al. "Synthesis and characterization of hexagonal boron nitride film as a dielectric layer for graphene devices." *ACS nano* 6.10 (2012): 8583-8590.

[4] Manchanda, L., and M. Gurvitch. "Yttrium oxide/silicon dioxide: a new dielectric structure for VLSI/ULSI circuits." *IEEE electron device letters* 9.4 (1988): 180-182.

[5] Kostoglou, Nikolaos, Kyriaki Polychronopoulou, and Claus Rebholz. "Thermal and chemical stability of hexagonal boron nitride (h-BN) nanoplatelets." *Vacuum* 112 (2015): 42-45.

[6] Dean, Cory R., et al. "Boron nitride substrates for high-quality graphene electronics." *Nature nanotechnology* 5.10 (2010): 722.

[7] Koma, Atsushi. "Van der Waals epitaxy for highly lattice-mismatched systems." *Journal of crystal growth* 201 (1999): 236-241.

[8] Giovannetti, Gianluca, et al. "Substrate-induced band gap in graphene on hexagonal boron nitride: Ab initio density functional calculations." *Physical Review B* 76.7 (2007): 073103.

[9] Lee, Gwan-Hyoung, et al. "Electron tunneling through atomically flat and ultrathin hexagonal boron nitride." *Applied physics letters* 99.24 (2011): 243114.

[10] Britnell, Liam, et al. "Electron tunneling through ultrathin boron nitride crystalline barriers." *Nano letters* 12.3 (2012): 1707-1710.

[11] Li, Lu Hua, et al. "Strong oxidation resistance of atomically thin boron nitride nanosheets." *ACS nano* 8.2 (2014): 1457-1462.

[12] Zhi, Chunyi, et al. "Large-scale fabrication of boron nitride nanosheets and their utilization in polymeric composites with improved thermal and mechanical properties." *Advanced Materials* 21.28 (2009): 2889-2893.

[13] Gorbachev, Roman V., et al. "Hunting for monolayer boron nitride: optical and Raman signatures." *Small* 7.4 (2011): 465-468.

[14] Jacob, Zubin. "Nanophotonics: hyperbolic phonon–polaritons." *Nature materials* 13.12 (2014): 1081.

[15] Li, Lu Hua, and Ying Chen. "Superhydrophobic properties of nonaligned boron nitride nanotube films." *Langmuir* 26.7 (2009): 5135-5140.

[16] Yamakov, Vesselin, et al. "Piezoelectric and elastic properties of multiwall boron-nitride nanotubes and their fibers: A molecular dynamics study." *Computational Materials Science* 135 (2017): 29-42.

[17] Watanabe, Kenji, et al. "Far-ultraviolet plane-emission handheld device based on hexagonal boron nitride." *Nature photonics*3.10 (2009): 591.

[18] Li, Qi, et al. "High energy and power density capacitors from solution-processed ternary ferroelectric polymer nanocomposites." *Advanced Materials* 26.36 (2014): 6244-6249.

[19] Puglisi, Francesco Maria, et al. "2D h-BN based RRAM devices." *2016 IEEE International Electron Devices Meeting (IEDM)*. IEEE, 2016.

[20] Fang, Haoming, Shu-Lin Bai, and Ching Ping Wong. "Thermal, mechanical and dielectric properties of flexible BN foam and BN nanosheets reinforced polymer composites for electronic packaging application." *Composites Part A: Applied Science and Manufacturing* 100 (2017): 71-80.

[21] Oh, Keun-Hwan, et al. "Enhanced durability of polymer electrolyte membrane fuel cells by functionalized 2D boron nitride nanoflakes." *ACS applied materials & interfaces* 6.10 (2014): 7751-7758.

[22] Lu, Tun, et al. "Hexagonal boron nitride nanoplates as emerging biological nanovectors and their potential applications in biomedicine." *Journal of Materials Chemistry B* 4.36 (2016): 6103-6110.

[23] Pacile, D., et al. "The two-dimensional phase of boron nitride: Few-atomic-layer sheets and suspended membranes." *Applied Physics Letters* 92.13 (2008): 133107.

[24] Han, Wei-Qiang, et al. "Structure of chemically derived mono-and few-atomic-layer boron nitride sheets." *Applied Physics Letters* 93.22 (2008): 223103.

[25] Paffett, M. T., et al. "Borazine adsorption and decomposition at Pt (111) and Ru (001) surfaces." *Surface Science* 232.3 (1990): 286-296.

[26] Wang, Li, et al. "Epitaxial growth of a 100-square-centimetre single-crystal hexagonal boron nitride monolayer on copper." *Nature* 570.7759 (2019): 91.

[27] Zeng, Zhiyuan, et al. "An effective method for the fabrication of few-layer-thick inorganic nanosheets." *Angewandte Chemie International Edition* 51.36 (2012): 9052-9056.

[28] Sutter, P., et al. "Scalable synthesis of uniform few-layer hexagonal boron nitride dielectric films." *Nano letters* 13.1 (2012): 276-281.

[29] Xu, Mingsheng, et al. "Formation of monolayer and few-layer hexagonal boron nitride nanosheets via surface segregation." *Nanoscale* 3.7 (2011): 2854-2858.

[30] Glavin, Nicholas R., et al. "Synthesis of few-layer, large area hexagonal-boron nitride by pulsed laser deposition." *Thin Solid Films* 572 (2014): 245-250.

[31] Xiong, Jun, et al. "Carbon-doped porous boron nitride: metal-free adsorbents for sulfur removal from fuels." *Journal of Materials Chemistry A* 3.24 (2015): 12738-12747.

[32] Zeng, Haibo, et al. "“White graphenes”: boron nitride nanoribbons via boron nitride nanotube unwrapping." *Nano letters* 10.12 (2010): 5049-5055.

[33] Zuo, Zheng, et al. "In-situ epitaxial growth of graphene/h-BN van der Waals heterostructures by molecular beam epitaxy." *Scientific reports* 5 (2015): 14760.

[34] Zheng, Renjing, et al. "Low-temperature growth of graphene on iron substrate by molecular beam epitaxy." *Thin Solid Films* 627 (2017): 39-43.

[35] Tian, Hao, et al. "Role of Carbon Interstitials in Transition Metal Substrates on Controllable Synthesis of High-Quality Large-Area Two-Dimensional Hexagonal Boron Nitride Layers." *Nano letters* 18.6 (2018): 3352-3361.

[36] Khanaki, Alireza, et al. "Effect of high carbon incorporation in Co substrates on the epitaxy of hexagonal boron nitride/graphene heterostructures." *Nanotechnology* 29.3 (2017): 035602.

[37] He, Yanwei, et al. "Large-area adlayer-free single-layer h-BN film achieved by controlling intercalation growth." Applied Surface Science 498 (2019): 143851.

[38] Tian, Hao, et al. "Growth Dynamics of Millimeter - Sized Single - Crystal Hexagonal Boron Nitride Monolayers on Secondary Recrystallized Ni (100) Substrates." Advanced Materials Interfaces (2019).

Chapter 2. Direct tunneling and dielectric breakdown study of monolayer h-BN

2.1 Introduction and overview

In spite of the fact that h-BN is an ideal insulator for layered channel materials, the usage of h-BN as dielectrics is still at a very early stage, therefore a profound study of h-BN performance as a dielectric material is critical.

So far, for the dielectric property study of h-BN films, Lee et al. [1] reported that the tunneling transport in thick mechanically exfoliated h-BN films are normally dominated by Fowler-Nordheim (F-N) conduction, while single, bi-, and tri-layer films polarized at a low bias are attributed to direct tunneling (DT). Similar conclusions are extracted from exfoliated BN nanosheets by Britnell et al. [2], who further identified the absence of pinholes and dangling bonds by means of conductive atomic force microscope (CAFM). The dielectric strength reported of large area CVD-grown h-BN films ranges between 1.5 MV/cm [3] and 12 MV/cm [4]. In terms of dielectric breakdown (BD) mechanism study, the percolation model [5] is the most accepted theory for BD formation for 3D insulators, and it states that the insulating capability is lost because of the formation of a defective conductive nanofilament (CNF) connecting the two sides of the dielectric (shown in Figure 2.1). The dielectric breakdown for the high-k oxides on SiO_2[7] and graphene [8] also follows the percolation model. But whether the model works on single layer 2D materials still need to study. For the identification of soft breakdown (SBD), two conventional representative SBD Current-Voltage (I-V) characteristics are given in Figure 2.2 [9], which are actually incomplete definition and require further study. For the breakdown mechanism study of h-BN, 2D layered h-BN is widely studied [10-15], layer-by-layer

breakdown [10] and hard breakdown theory [15] are reported. Nevertheless, deep investigation on soft breakdown (SBD), reversibility and reliability of ultrathin MBE grown h-BN film, especially monolayer film is still quite limited.

In this chapter, we report our thorough study of dielectric property of monolayer h-BN grown by MBE. In this work, we fabricate scalable MIM (Metal-Insulator-Metal) devices on monolayer h-BN film grown by MBE by using standard photolithography, E-beam evaporating, lift-off, and plasma etching process. By the means of measuring the successive I-V (Current- Voltage), voltage sweep I-V, TDDB (Time-dependent Dielectric Breakdown) behaviors by probe station, we find the highest soft breakdown (SBD) compliance current (CC) ever reported, prove ultra-high dielectric strength and durability of h-BN film, differentiate SBD and HBD, analyze the tunneling mechanism and recovery mechanism and propose breakdown model based on statistical data analysis, especially Weibull distribution analysis.

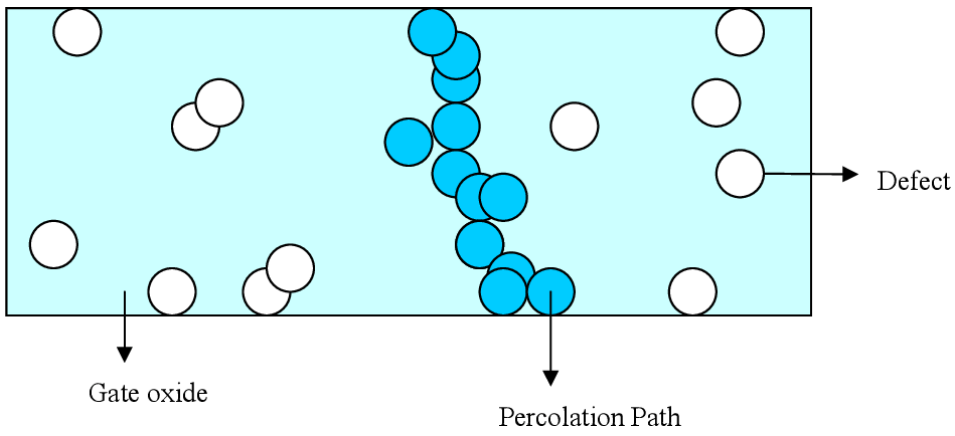

Figure 2.1 Schematic of a percolation model for gate oxide breakdown. [6]

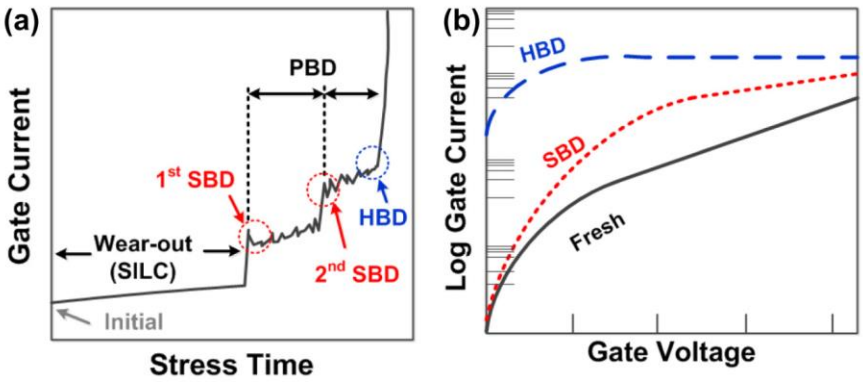

Figure 2.2 (a) A typical behavior of gate leakage current with an increase in stress time and (b) typical I–V characteristics during stress [9].

2.2 H-BN film growth condition and nanoscale characterization

The growth conditions details of three h-BN samples used in this study grown on Ni foil substrates are summarized in Table 2.1, the corresponding nanoscale characterization results are shown in Figure 2.3 and Figure 2.4.

Step	Parameters	Sample 1	Sample 2	Sample 3
Hydrogen Annealing	Substrate	Ni	Ni	Ni
	Substrate temperature [^{o}C]	927	960	930
	Hydrogen gas flow [sccm]	10	10	10
	Duration [mins]	15	60	15
Carburization	Acetylene gas flow [sccm]	0.5	0.5	0.5
	Duration [s]	300	300	240
	Substrate temperature [^{o}C]	927	900	930
H-BN Growth	Substrate temperature [^{o}C]	927	900	930
	Boron cell temperature [^{o}C]	1170	1120	1170
	Ammonia gas flow [sccm]	5	5	4
	Nitrogen gas flow [sccm]	10	-	8
	Nitrogen ECR current [mA]	60	-	60
	Duration [hours]	7	8	6

Table 2.1 Summary of growth conditions for three monolayer h-BN samples.

Figure 2.3 summarizes the characterization of sample 1. Fig. 2.3(a) shows an SEM image of single-layer film taken at the center of as grown sample 1, demonstrating continuous film. The inset displays the edge area of the film, where some discrete h-BN flakes and Ni substrate are seen. Fig. 2.3 (b) shows an optical microscopy image of the transferred h-BN film on SiO_2/Si substrate, with uniform contrast in large area despite of some small contaminations (black and yellow dots), indicating high film quality. The AFM image in Fig. 2.3 (c) was taken on the transferred h-BN film. The inset reveals a scanning profile across the sample edge, showing a step height of about 0.6 nm. Compared to theoretical thickness 0.33 nm of single-layer film, the larger value may be caused by different atomic forces between tip/h-BN and tip/SiO_2, weak binding between h-BN film and SiO_2/Si substrate, as well as water and gases intercalated in the interface [16]. Raman spectrum was then obtained on the transferred sample as shown in Fig 2.3(d). An E_{2g} phonon mode at 1370 cm^{-1} can be found in the Raman spectrum, corresponding to monolayer h-BN [17]. UV–vis absorption spectrum was carried out on transferred sample onto a sapphire substrate. A strong peak shown in Fig. 2.3 (e) at 202 nm with a sharp absorption edge can be observed, corresponding to a bandgap of 6.02 eV for h-BN extracted from the Tauc equation for a direct bandgap (inset in Fig. 2.3 (e)).[18] The XPS tested on as-grown sample further confirms the existence and stoichiometry of h-BN. The binding energies of B 1s and N 1s are shown to be at 190.1 and 397.6 eV, respectively (Fig 2.3 (f)), which is an indication of sp^2 bonds and consistent with other reports [19,20].

Figure 2.4 shows the characterization of the other 2 monolayer h-BN films. Fig.2.4 (a), (b) are SEM images of as grown h-BN film on Ni substrate of sample 2 and 3, respectively, insets reveal the edge area of

the samples, showing boundary between film and substrate. Raman spectra (Fig2.4 (c)) extracted on the transferred h-BN films from sample 2 and 3 on SiO_2/Si demonstrate evident monolayer h-BN peak at 1370cm^{-1}. AFM images across h-BN flake edge taken on transferred sample 2 and sample 3 are shown in Fig. 2.4 (d) and (e), respectively, indicating thickness 0.6nm. Absorption spectra of h-BN films of samples 2 and 3 were performed on transferred sample with sapphire substrate (Fig. 2.4(f)) reveal strong 202nm peak.

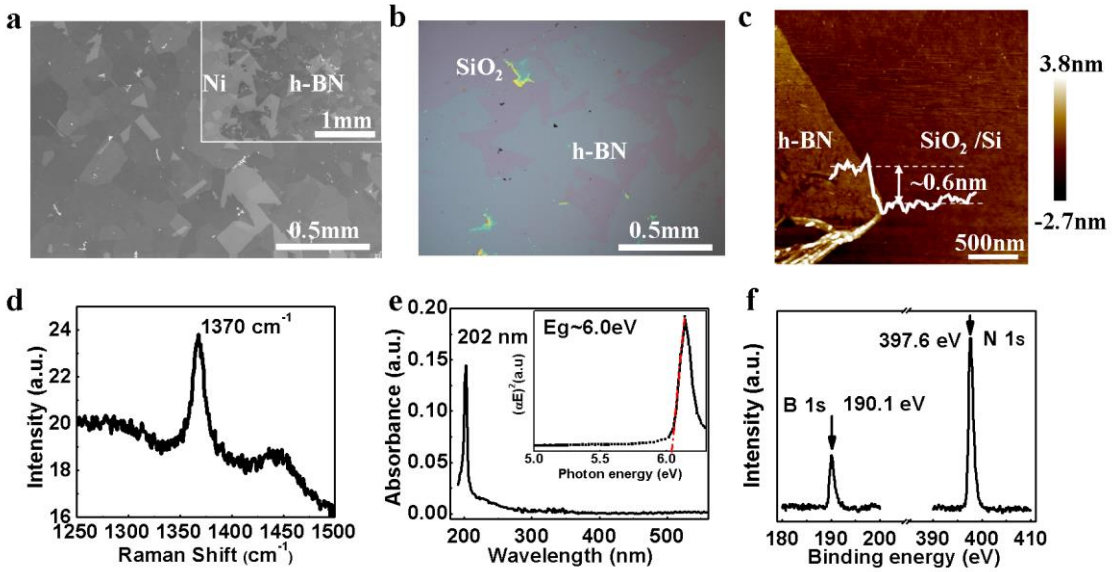

Figure 2.3 Characterization of h-BN monolayer (Sample 1). (a) SEM image of the sample, showing continuous h-BN film on Ni substrate, inset displays the edge area of the film, where some discrete h-BN flakes and Ni substrate are seen. (b) Optical microscope image of transferred h-BN on SiO_2/Si substrate. (c) AFM image of the transferred h-BN film near an edge of the film. The inset is a scanning profile across the sample edge, showing a step height of about 0.6 nm. (d) Raman spectrum of the transferred h-BN on SiO_2/Si, showing a characteristics E_{2g} phonon peak at 1370 cm^{-1}. (e) Absorption spectrum of h-BN film transferred onto a sapphire substrate. Inset shows the Tauc plot determining the bandgap of the h-BN to be about 6. 0 eV. (f) XPS spectrum of B 1s and N 1s signals at 190.1 eV and 397.6 eV, respectively.

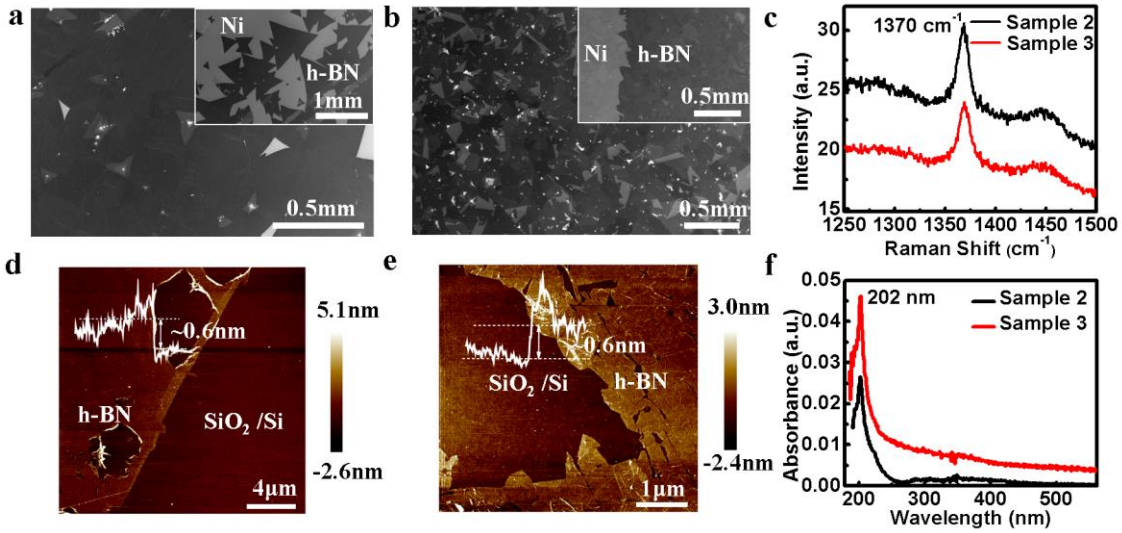

Figure 2.4 Characterization of the other 2 monolayer h-BN films. (a), (b) SEM images of h-BN film on Ni substrate of sample 2 and 3, respectively, insets show the edge area of the samples, showing boundary between film and substrate. (c) Raman spectra of the transferred h-BN films from sample 2 and 3 on SiO_2/Si. (d), (e) AFM images across h-BN flake edge of transferred sample 2 and sample 3, respectively. (f) Absorption spectra of h-BN films of samples 2 and 3 transferred onto a sapphire substrate.

2.3 Electrical and dielectric characteristics

The typical breakdown Current-Voltage (I-V) characteristics, multiple soft breakdown (SBD) performance, self-recovery I-V phenomenon and successive I-t behaviors are demonstrated in this part.

2.3.1 Breakdown Current-Voltage characteristics

Figure 2.5(a) shows a typical I-V characteristic of a device with a size of 25 ×25 μm^2. Figure 2.5(b) shows a cross sectional view of a Ni/h-BN/Ni device and a bright-field OM image of a device with a size of 100×100 μm^2.In terms of I-V characteristics, the breakdown generally undergoes two consecutive stages as shown in Figure 2.5 (a).

The beginning phase is charged carriers tunneling stage as charges start flowing as long as voltage stress is applied on the device, and consequently, current goes up gradually. The second stage is the BD

phenomenon which takes place when a critical degree of degradation is locally reached. When applied voltage reaches the saturation voltage the film can endure, the device loses dielectric property and turns into electrically conductive so current abruptly increases to the compliance current, in our case, the maximum current of the equipment 0.1A. The moment of transient conduction switch is defined as BD point and the current and voltage read at the particular point is regarded as I_{BD} (breakdown current) and V_{BD} (breakdown voltage), respectively.

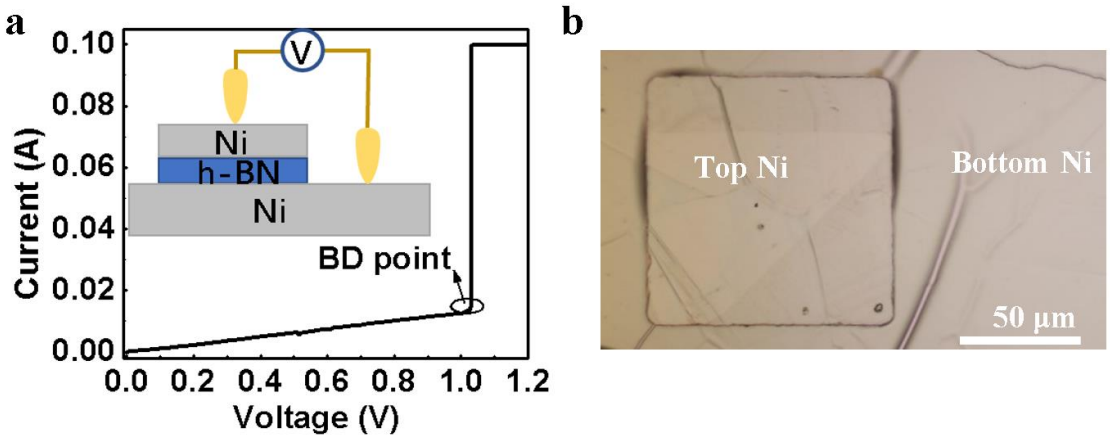

Figure 2.5 (a) Current-Voltage (I-V) characteristic of an Ni/h-BN/Ni device of size A1 with a compliance current of 100 mA. Dielectric breakdown at a voltage of ~ 1.0 V is demonstrated. Inset is a schematic of the MIM device. (b) Top view OM image of a device with size A3.

2.3.2 Multiple SBD performance

Unlike conventional phenomena that single breakdown can lead to physical damage and complete conduction of insulator, we found that our MIM devices based on monolayer h-BN can endure more than once and up to 85 times breakdown events before worn out under 100mA compliance current (Figure 2.6 (a)).The 1st to 85th curves display typical I-V characteristics of a MIM device, namely the current increases monotonously as the increase of the bias until breakdown when it sharply increases and reaches the

compliance current. The I-V curves from 86^{th} to 91^{st} become linear and the currents increase sharply and quickly reach the compliance current level, suggesting that the device is totally conductive, thus is physically worn out, and cannot be recovered. The reversible and repeatable breakdown events for the first 85-operations can be regarded as soft breakdown (SBD), after which physically hard breakdown (HBD) is reached.

The SBD involves the passing of large amount of currents through conductive paths. This process generates large joule heat locally, which supplies energy to nearby atoms in both h-BN and adjacent Ni electrodes, leading to lateral BD spot propagation and electromigration. Further repeated SBD operations ultimately create permanent conduction paths and dramatic failure of the device. The fact that the device can endure DC voltage sweep and undergo breakdown events up to 85 times suggests that the h-BN monolayer is electrically robust.

Figure 2.6 b shows cumulative distribution diagram of breakdown voltages and breakdown currents in the test sequence of the corresponding device. The change of V_{BD} and I_{BD} with the test sequence is random and stochastic. However, breakdown voltages and breakdown currents stably center around 1.21 V, and 0.056 A, respectively, as the test sequence goes on, indicating high reliability of the device.

It is worth mentioning that previously reported SBD behaviors in other dielectric films refer to either abrupt pre-degradation before HBD or breakdown with a small compliance current [9,21]. Both scenarios indicate that the SBD I_{BD} values are smaller than that of HBD. Here, the currents going through the h-BN monolayers via recoverable SBD processes are the same as that of the irrecoverable HBD, which are limited by the large compliance current of 100 mA. Thus, the identification of whether the breakdown is SBD or

HBD only depends on the recoverability of the devices. In literature [22], BD behaviors with a BD current at a level of only a few mA were already treated as irrecoverable HBD. The fact that the h-BN monolayer devices here do not breakdown until a BD current of ~60 mA and can further sustain 100-mA compliance currents, and still recover, revealing ultrahigh dielectric strength of the h-BN monolayers compared with other dielectric materials.

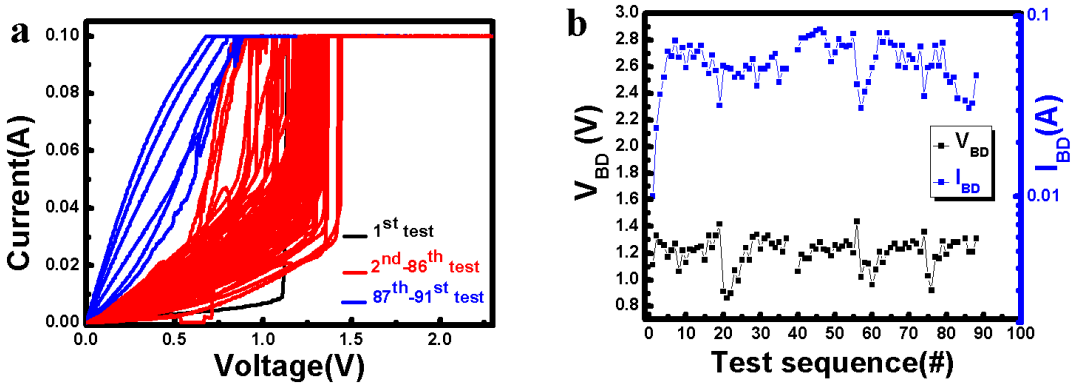

Figure 2.6 (a) I-V characteristics of a Ni/h-BN/Ni device of 50×50 μm^2 with 91 successive operations. (b) Distribution of the BD voltages and BD currents of the device within the first 85-BD cycles.

2.3.3 Successive I-t performance

The successive time dependence of the current (I-t) prior to and after SBD events under constant biases was carried out to further understand the BD mechanism and reliability of the Ni/h-BN/Ni devices. Figure 2.7 shows a typical result of a device with a size of 50×50 μm^2. The device was firstly biased at 0.5 V, the I-t curve shows abrupt random fluctuations around a current of about 30 mA. The fluctuation is a type of random telegraph noise signal, which is an indication of the trapping and de-trapping of charges in the h-BN monolayer [23]. Then 0.8 V was applied to the device, at which the current quickly increases to the compliance current, indicating the breakdown of the device. Lastly, a voltage of 0.5 V was applied to the

device again. The I-t curve is very similar to the initial state, which confirms good self-healing property of the device after SBD at 0.8 V.

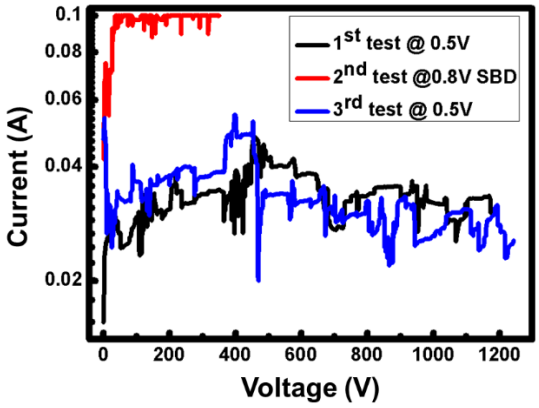

Figure 2.7 3 successive I-t curves collected with respect to a certain constant voltage stress.

2.3.4 Self-recovery I-V characteristics

The device recovery was further studied by performing voltage sweep operations. Figure 2.8 shows I-V characteristics of two complementary recovery results. Both characteristics exhibit polarity independent. Forward sweeps in both polarities ensured the device to undergo SBD events and then backward sweeps allow the bias to linearly scale back to zero. In one case as shown in Figure 2.8 (a), the currents in the backward sweeps almost linearly decrease as the decrease of the bias and the device is completely recovered to original state once stress is released. Figure 2.8 (b) demonstrates that the currents abruptly drop and the device returns to original state as the backward voltage reduces but before the bias is totally released, which is a typical threshold resistive switching characteristic. The recovery characteristics demonstrated in both Figure 2.8 and Figure 2.6 may be understood as follows: the h-BN film may have some intrinsic and extended defects such as boron or nitrogen vacancies, and grain boundaries. Additional defects are generated in the

film as the conductive paths are formed during the BD process. These defects have been de-trapped due to enormous Joule heat generated during the BD. As the applied bias is reduced or relieved, the heat generation becomes less. In the meantime, since both monolayer h-BN [24, 25] and Ni [26] have high thermal conductivities, the dissipation of the generated heat is efficient. Thus charges can quickly fill the de-trapped defects and the film can recover from SBD state to the original state [27]. Another reason of device recovery can be related to the electric field across the film. As the electric field is reduced or relieved, trapped charges, in particular, deeply trapped charges are more difficult to de-trap.

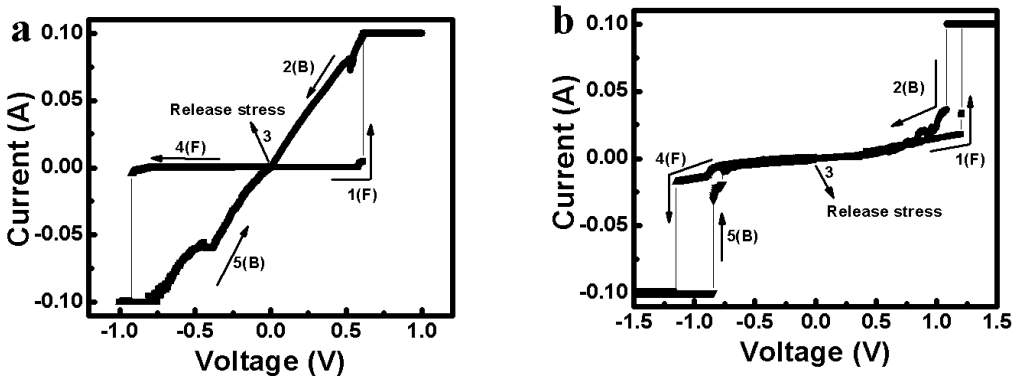

Figure 2.8 (a), (b) I-V characteristics of Ni/h-BN/Ni devices of 50×50 μm^2 operated by sweeping bias, demonstrating two typical self-recovery behaviors.

2.4 Data analysis and discussions

Based on the breakdown dielectric behaviors collected, carrier tunneling and breakdown voltage distributions are statistically analyzed and the corresponding mechanisms are discussed. The electron tunneling processes including tunneling mechanism, current amplitude and area-dependence are presented. The area-dependent V_{BD} distributions, distinct peak value and breakdown mechanism are studied mainly by Weibull distributions analysis.

2.4.1 Electron tunneling

From the summary of BD I-V curves of Ni-monolayer h-BN-Ni arranged by size shown in Figure 2.9 (a)-(d), the dominated tunneling processes can be identified. Generally, the current increases linearly as the increase of the bias, suggesting that the device is operated under direct tunneling (DT) region under small and moderate voltages [28, 29]. The current bumps and sudden increase especially at higher bias region are apparently caused by trap/de-trap, which indicates trap-assisted tunneling also plays an important role in the tunneling mechanism [30 45]. The corresponding simple schematic of the band structure of the MIM device is given in Figure 2.9 (e).

Figure 2.8 (f) shows cumulative probability of DT currents at a bias of 0.1 V for the devices with all four sizes. Since the tunneling currents span a wide range (summarized in Table 1), the most probable DT currents or peak currents ($\mathbf{I}_{peak}$) at 0.1 V are obtained by setting the cumulative probability at 63.2%. $\mathbf{I}_{peak}$ values for the devices with the four sizes are also summarized in Table 1. These currents are comparable with that from the tunneling devices based on CVD grown [31] and exfoliated [32] h-BN monolayers. The inset of Figure 2.8(f) shows $\mathbf{I}_{peak}$ as a function of device area. Although $\mathbf{I}_{peak}$ increases as the increase of the device area, it tends to saturate in larger devices, namely, the relationship is surprisingly not linear.

To clarify this intriguing phenomenon, we hypothesize that the electron tunneling occurs only in an effectively local small area (A_{eff}) instead of through the entire device area (A_{device}) in these atomic layer tunneling devices, especially with very large A_{device}. To prove this hypothesis, one way is to calculate the tunneling current through existing model [28,29] and compare the values with the experimental data.

Schottky barrier height of Ni/h-BN junction Φ_B is assumed to be 3.0 eV [33], which was also observed between h-BN and other metals [32, 34]. The barrier width d, namely the thickness of h-BN monolayer is 0.66 nm assuming this is the van der Waals distance between the h-BN and top/bottom Ni contacts [35]. Under a small applied bias of 0.1 V, the DT mechanism dominates the electron tunneling process. The DT current is expressed as [28, 29]:

$$\mathrm{I(V,T)} = \mathrm{I(V,0)} \times \left\{1 + \left[\frac{3\times10^{-9}(dT)^2}{\Phi_B/q}\right]\right\}, \qquad (1)$$

where $\mathrm{I(V,0)} = \frac{A_{eff}\sqrt{2m\Phi_B}q^2V}{h^2d}\exp\left(\frac{-4\pi d\sqrt{2m\Phi_B}}{h}\right)$, m is electron effective mass, which is 0.26 m_0 [36], h is Plank's constant, q is fundamental charge, and d is expressed in angstroms. $I(V,0)$ is well-known Simmons DT current for an MIM device at absolute temperature of 0 K, and the terms in the {} bracket modify $I(V,0)$ to $I(V,T)$, a DT current at a temperature of T, which is 300 K here. Based on the I_{peak} values at 0.1 V, the effective areas A_{eff} for electron tunneling in devices A1-A4 are calculated and summarized in Table 1. The effective areas are found to be orders of magnitude smaller than physical areas of the devices, respectively. This proves that the electron tunneling indeed goes through a surprisingly much smaller local area, namely, electrons do not flow through a great deal of remaining device areas during the operation, which are somewhat inactive.

Similar phenomenon was also observed in other tunneling devices, such as Al/AlO_X/Al tunneling junctions [37], and magnetic tunneling junctions [38]. The appearance of these "hot spot" tunneling was explained to be partially due to uneven thickness of the films [37,38]. In our samples, although there are some multi-layered island adlayer structures shown as white features in these SEM images, which shall not carry

tunneling currents compared with monolayers due to thicker barriers, majority of areas have h-BN monolayers because the percentage of occupied areas by these adlayers is very low. Thus, the contribution from non-uniform film thickness in our devices could be negligible. A much smaller effective area for electron tunneling could originate from the existence of non-uniform gap distances between single h-BN layer and Ni (both top contact metal and bottom Ni substrate). During the h-BN growth at high temperature, the film may largely conform onto the relatively flat surface, nevertheless, when the substrate temperature decreases to room temperature, uneven gaps may be formed due to different expansion coefficients of Ni and h-BN. In addition, since the deposition of Ni onto h-BN to form top metal contact is done at room temperature, those Ni atoms nearest to the h-BN plane may not conform onto the h-BN monolayer with the same distance across the entire surface. Further experiments such as high-resolution transmission electron microscopic technique may be necessary to elucidate the hypothesis.

Device	A_{device} **[μm²]**	**n**	$I_{tunneling}$ **range [mA]**	I_{peak} **[mA]**	$A_{effective}$ **[μm²]**
A1	25×25	97	1.7×10^{-3} ~ 21	1.6	0.148
A2	50×50	96	2.5×10^{-4}~19	2.4	0.221
A3	100×100	30	9.6×10^{-5}~ 8	3.1	0.286
A4	200×200	50	1.9×10^{-3}~ 1.5	3.3	0.304

Table 2.2 Tunneling current summary and analysis including experiment data collected at 0.1 V of all Ni/h-BN/Ni devices with four different areas. The effective device areas A_{eff} were calculated from the DT formula.

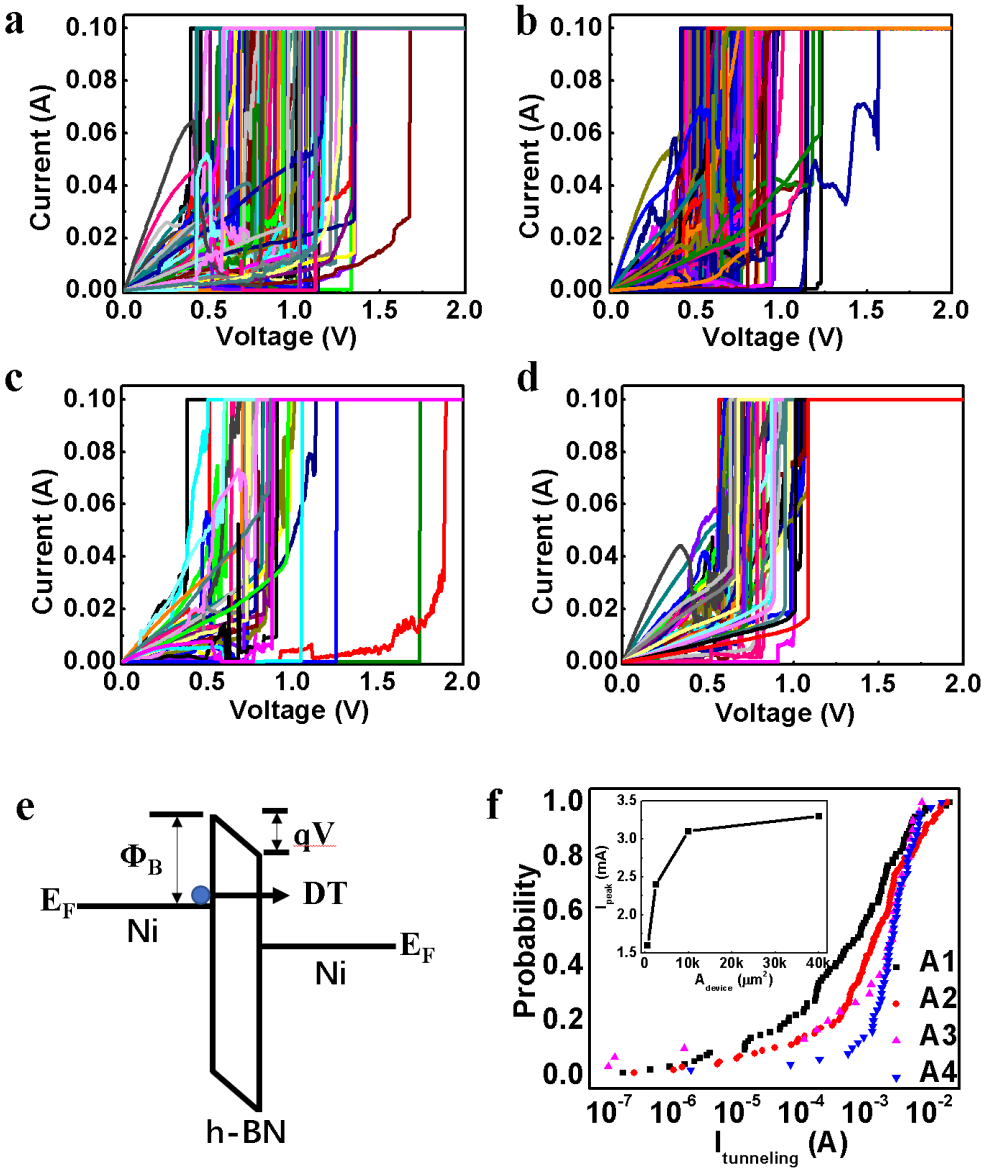

Figure 2.9 (a)I-V curves of 97 devices with an area of 25 × 25 μm^2. (b) I-V curves of 96 devices with an area of 50 × 50 μm^2. (c) I-V curves of 30 devices with an area of 100 × 100 μm^2. (d) I-V curves of 50 devices with an area of 200 × 200 μm^2. (e) Schematic of direct tunneling mechanism of Ni/h-BN/Ni device. (f) The cumulative probability distribution of $I_{tunneling}$ with different device areas. All tunneling currents were collected at a bias of 0.1 V. Black, red, magenta and blue symbols represent devices with size 25×25, 50×50, 100×100 and 200×200 μm^2, respectively. The inset is the peak tunneling current ($\mathbf{I}_{peak}$) as a function of device area, where $\mathbf{I}_{peak}$ is the 63% of cumulative current value. Tunneling current being not linearly proportional to device area is evident.

2.4.2 Dielectric breakdown voltage distribution

Figure 2.10 (a) shows histogram of breakdown voltage distribution of devices with four different sizes. A Gaussian distribution fittings were performed, and the breakdown voltage ranges and peak breakdown voltages are summarized in Table 2.3. Nevertheless, the coefficients of determination R^2 summarized in the Table as well are generally smaller than 0.9. This means that not all the breakdown voltages can be fitted into the perfect Gaussian distribution. To address this issue, Weibull distribution analysis [39] was performed. The cumulative failure probability F can be calculated from:

$$F = \frac{n}{N+1}, \qquad (2)$$

where n=1, 2, …, N is the number of broken-down devices, and N is total number of the devices. Fig. 3b shows cumulative failure probability as a function of breakdown voltage for all A1-A4 devices. From the plot, the most probable breakdown voltage or peak voltage α_F, which is defined as the voltage, at which 63.2% of devices have broken down, is obtained for A1-A4 devices and summarized in Table 2.3. These values differ for different devices sizes and also slightly different with that obtained from Gaussian fitting.

To further clarify the area-dependent breakdown characteristics and elucidate the breakdown mechanism, the cumulative failure probability F can be described using so-called Weibull cumulative distribution function F (V_{BD}), which is defined as

$$\mathrm{F}(V_{BD}) = 1 - \exp\left[-\left(\frac{V_{BD}}{\alpha}\right)^{\beta}\right], \qquad (3)$$

where α is the most probable breakdown voltage, which is also referred as Weibull scale parameter, and β, the shape parameter, is the Weibull modulus indicating the width of the distribution, namely it characterizes

the degree of V_{BD} variation (uniformity), leading to the determination of the failure mode classification. The Weibull cumulative distribution function can be rearranged by taking two logarithms:

$$\ln[-\ln(1-\mathrm{F})] = \beta\ln(V_{BD}) - \beta\ln\alpha, \qquad (4)$$

Thus the Weibull plot of ln [-ln (1- F)] versus $\ln(V_{BD})$ can be used to extract the slope β, and α from the y-intercept, -β lnα. Assuming the breakdown goes through defect, and these defects are randomly distributed across the entire areas of the devices, the breakdown voltages would follow an area-scaling law [40]:

$$\frac{V_{BDm}}{V_{BDn}} = \left[\frac{A_n}{A_m}\right]^{1/\beta}, \qquad (5)$$

where A_m, and A_n are devices with arbitrary sizes. The corresponding area-scaling Weibull plot for devices with different areas is derived as [40]:

$$\ln[-\ln(1-F_m)] - \ln[-\ln(1-F_n)] = \ln(A_m/A_n), \qquad (6)$$

Thus the Weibull plot data have identical β, and the fitted lines will overlap if scaled by $ln(A_m/A_n)$.

Figure 2.10(c) shows the Weibull plots of A1-A4 devices. The α and β values are summarized in Table 2.3. It is evident that Weibull plots for A1-A3 devices in the entire breakdown voltage ranges and for A4 device in the higher breakdown voltage range have similar β values ($3.36<\beta<3.98$), indicating identical intrinsic breakdown mechanism through randomly distributed defects [41]. Much larger β value of 9.34 is also extracted for A4 device in the lower breakdown voltage range, which suggests the deviation from the intrinsic breakdown mechanism and emergence of new breakdown paths [42]. The α values are very similar to the breakdown voltages obtained from cumulative failure probability analysis in Fig. 2.10 (b), suggesting that the two methods are complementary to each other for reliably extracting the peak breakdown voltages.

Figure 2.10(d) shows normalized Weibull plots after scaling effective areas to a common area of 1 μm^2. Data points for normalized A1-A3 devices in almost entire range of the breakdown voltages and normalized A4 devices in the higher voltage range overlap well. Nevertheless, normalized Weibull plots after scaling the physical areas of the devices (A1-A4) to a common area of 1 μm^2 do not overlap. This noticeable difference further demonstrates that the devices operate across only small effective areas rather than entire physical areas of the devices. Furthermore, it implies that the breakdown locations are randomly distributed.

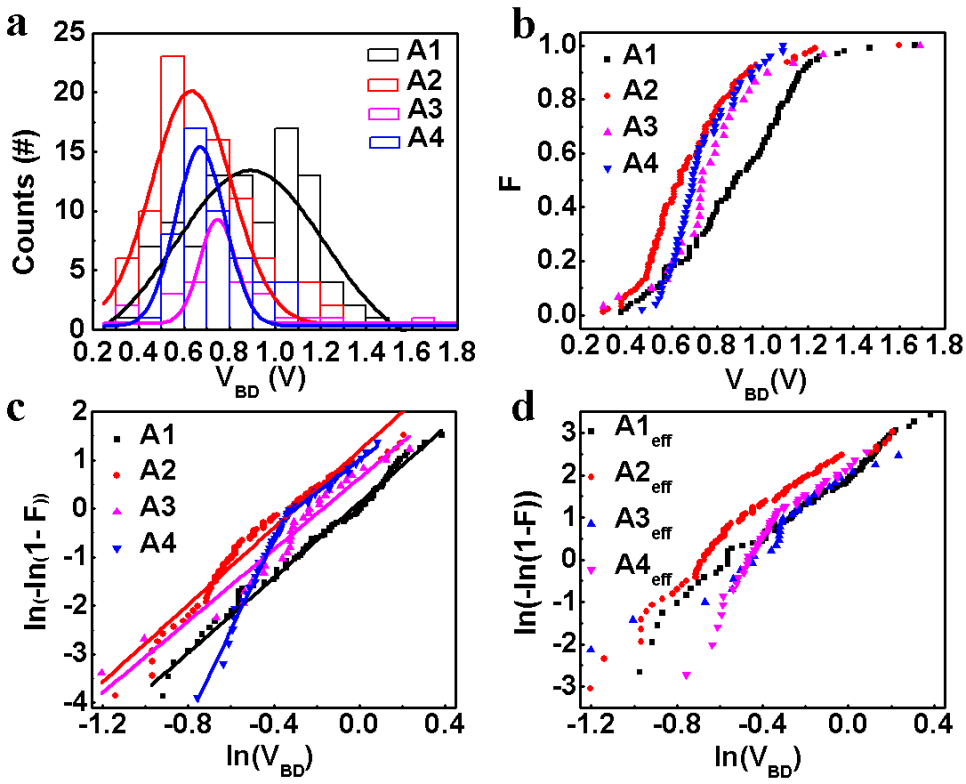

Figure 2.10 (a) Histogram of breakdown voltage distribution with a bin size of 0.1 V and relevant Gaussian distribution fittings. (b) Cumulative failure probability F as a function of V_{BD}. (c) Weibull plot of breakdown voltage distribution. (d) Normalized Weibull plot by scaling effective areas A_{eff} to 1 μm^2. Data overlapping for $A1_{eff}$-$A3_{eff}$ in most of breakdown voltage ranges and $A4_{eff}$ at higher voltage range is acceptable.

As seen from Table 2.2, the effective area generally increases as the increase of the physical areas, however, it tends to saturate. For example, as the device area increases from 100×100 μm^2 to 200×200 μm^2, the effective area only increases from 0.286 μm^2 to 0.304 μm^2, namely about only 6.3%. According to the breakdown voltage area-scaling law (Eq. 5), the breakdown voltage will saturate as the device area increases. Thus it is reasonable to designate the minimum breakdown voltages in all present studied devices to be that of the devices of 200×200 μm^2, which is ~0.78 V according to Weibull analysis. Accordingly, the minimum effective breakdown electric field (E_{BD}) can be determined to be 11.8 MV/cm, which is comparable with that of thick high-quality SiO_2.

Device	V_{BD} range [V]	Peak V_{BD} (Gauss) [V]	R^2 (Gauss)	α_F [V]	$\alpha_{Weibull}$ [V]	β	R^2 (Weibull)
A1	0.38 ~ 1.67	0.90	0.74	1.00	0.97	3.87	0.99
A2	0.30 ~ 1.60	0.68	0.90	0.72	0.74	3.98	0.95
A3	0.30 ~ 1.70	0.75	0.83	0.79	0.84	3.69	0.94
A4	0.47 ~ 1.10	0.67	0.88	0.73	0.78	3.36/9.34	0.91

Table 2.3 The parameters of area-dependent breakdown voltage distribution as a result of Gaussian fitting and Weibull analysis of Ni/h-BN/Ni devices, where n represents number of samples, R^2 is coefficient of determination.

2.5 Conclusion

In this chapter, we have demonstrated a thorough study of the electrical properties of Ni/h-BN/Ni tunneling devices based on epitaxial h-BN monolayer films. The electron tunneling is dominated by direct

tunneling at lower biases and the electrons flow only through an effective area, which is much smaller than the physical area of the device. At a higher voltage, the devices undergo breakdown process. It is found that recoverable soft breakdown with extremely high compliance current of 100 mA dominants the failure behavior and can repeat up to 85 times before they are physically worn out, which indicates extraordinary endurance of h-BN monolayers. The Weibull analysis of the breakdown voltages suggests that the breakdown paths are randomly distributed and area-scaling law applies closely to the effective area rather than the physical area of the device. The minimum effective breakdown electric field is demonstrated to be 11.8 MV/cm, indicating high dielectric strength of the h-BN monolayers. Joule heat and electric field play important roles in the breakdown and recovery of the devices.

2.6 References

[1]. Lee, Gwan-Hyoung, et al. "Electron tunneling through atomically flat and ultrathin hexagonal boron nitride." *Applied physics letters* 99.24 (2011): 243114.

[2]. Britnell, Liam, et al. "Electron tunneling through ultrathin boron nitride crystalline barriers." *Nano letters* 12.3 (2012): 1707-1710.

[3]. Kim, Ki Kang, et al. "Synthesis and characterization of hexagonal boron nitride film as a dielectric layer for graphene devices." *ACS nano* 6.10 (2012): 8583-8590.

[4]. Hattori, Yoshiaki, et al. "Layer-by-layer dielectric breakdown of hexagonal boron nitride." *ACS nano* 9.1 (2014): 916-921.

[5]. Sune, J., et al. "On the breakdown statistics of very thin SiO2 films." *Thin solid films* 185.2 (1990): 347-362.

[6] Stathis, J. H. "Percolation models for gate oxide breakdown." *Journal of applied physics* 86.10 (1999): 5757-5766.

[7]. Obreja, V. V. N., et al. "Edge current induced failure of semiconductor PN junction during operation in the breakdown region of electrical characteristic." *Microelectronics Reliability*51.3 (2011): 536-542.

[8]. Uppal, H. J., et al. "Breakdown and degradation of ultrathin Hf-based (Hf O 2) x (Si O 2) 1− x gate oxide films." *Journal of Vacuum Science & Technology B: Microelectronics and Nanometer Structures Processing, Measurement, and Phenomena* 27.1 (2009): 443-447.

[9] Ho, Chih-Hsiang, Soo Youn Kim, and Kaushik Roy. "Ultra-thin dielectric breakdown in devices and circuits: A brief review." *Microelectronics Reliability* 55.2 (2015): 308-317.

[10]. Hattori, Yoshiaki, et al. "Layer-by-layer Dielectric Breakdown of Hexagonal Boron Nitride Film in Conductive AFM Measurement." *APS March Meeting Abstracts*. 2015.

[11]. Ji, Yanfeng, et al. "Boron nitride as two dimensional dielectric: Reliability and dielectric breakdown." *Applied Physics Letters*108.1 (2016): 012905.

[12] Hattori, Yoshiaki, et al. "Anisotropic dielectric breakdown strength of single crystal hexagonal boron nitride." *ACS applied materials & interfaces* 8.41 (2016): 27877-27884.

[13] Palumbo, Felix, et al. "Bimodal dielectric breakdown in electronic devices using chemical vapor deposited hexagonal boron nitride as dielectric." *Advanced Electronic Materials* 4.3 (2018): 1700506.

[14] Jiang, Lanlan, et al. "Dielectric breakdown in chemical vapor deposited hexagonal boron nitride." *ACS applied materials & interfaces* 9.45 (2017): 39758-39770.

[15] Ranjan, A., et al. "Mechanism of soft and hard breakdown in hexagonal boron nitride 2D dielectrics." 2018 IEEE International Reliability Physics Symposium (IRPS). IEEE, 2018.

[16]M.H. Khan, Z. Huang, F. Xiao, G. Casillas, Z. Chen, P.J. Molino, H.K. Liu, Synthesis of large and few atomic layers of hexagonal boron nitride on melted copper, Sci. Rep. 5 (2015) 7743.

[17]R. Arenal, A. Ferrari, S. Reich, L. Wirtz, J.-Y. Mevellec, S. Lefrant, A. Rubio, A. Loiseau, Raman spectroscopy of single-wall boron nitride nanotubes, Nano Lett. 6 (2006) 1812–1816,

[18]Elias, Christine, et al. "Direct band-gap crossover in epitaxial monolayer boron nitride." Nature communications 10.1 (2019): 2639.

[19] P.R. Kidambi, R. Blume, J. Kling, J.B. Wagner, C. Baehtz, R.S. Weatherup, R. Schloegl, B.C. Bayer, S. Hofmann, In situ observations during chemical vapor deposition of hexagonal boron nitride on polycrystalline copper, Chem. Mater. 26 (2014) 6380–6392,

[20] S. Caneva, R.S. Weatherup, B.C. Bayer, R. Blume, A. Cabrero-Vilatela, P. Braeuninger-Weimer, M.-B. Martin, R. Wang, C. Baehtz, R. Schloegl, Controlling catalyst bulk reservoir effects for monolayer hexagonal boron nitride CVD, Nano Lett. 16 (2016) 1250–1261,

[21] Pompl, T., et al. "Soft breakdown and hard breakdown in ultra-thin oxides." Microelectronics reliability 41.4 (2001): 543-551.

[22] Takagi, S.-i.; Takayanagi, M. Carrier Transport Properties of Thin Gate Oxides After Soft and Hard Breakdown. *Microelectron. Eng.* 2001**,** *59*, 5-15.

[23] Jiang, Lanlan, et al. "Dielectric breakdown in chemical vapor deposited hexagonal boron nitride." *ACS applied materials & interfaces* 9.45 (2017): 39758-39770.

[24] Cai, Qiran, et al. "High thermal conductivity of high-quality monolayer boron nitride and its thermal expansion." *Science advances* 5.6 (2019): eaav0129.

[25] Gu, Xiaokun, and Ronggui Yang. "Phonon transport and thermal conductivity in two-dimensional materials." *Annual Review of Heat Transfer* 19 (2016).

[26] Xu, Zhongguang, et al. "Large-area growth of multi-layer hexagonal boron nitride on polished cobalt foils by plasma-assisted molecular beam epitaxy." *Scientific reports* 7 (2017): 43100.

[27] Sune, J., M. Nafria, and X. Aymerich. "Reversible dielectric breakdown of thin gate oxides in MOS devices." *Microelectronics Reliability* 33.7 (1993): 1031-1039.

[28] Simmons, John G. "Generalized formula for the electric tunnel effect between similar electrodes separated by a thin insulating film." *Journal of applied physics* 34.6 (1963): 1793-1803.

[29] Simmons, John G. "Generalized thermal J-V characteristic for the electric tunnel effect." *Journal of Applied Physics* 35.9 (1964): 2655-2658.

[30] Raghavan, Nagarajan, Kin Leong Pey, and Kalya Shubhakar. "High-κ dielectric breakdown in nanoscale logic devices–Scientific insight and technology impact." *Microelectronics Reliability* 54.5 (2014): 847-860.

[31] Ge, Ruijing, et al. "Towards Universal Non-Volatile Resistance Switching in Non-metallic Monolayer Atomic Sheets." *arXiv preprint arXiv:1709.04592* (2017).

[32] Lee, Gwan-Hyoung, et al. "Electron tunneling through atomically flat and ultrathin hexagonal boron nitride." *Applied physics letters* 99.24 (2011): 243114.

[33] Hattori, Yoshiaki, et al. "Determination of Carrier Polarity in Fowler–Nordheim Tunneling and Evidence of Fermi Level Pinning at the Hexagonal Boron Nitride/Metal Interface." *ACS applied materials & interfaces* 10.14 (2018): 11732-11738.

[34] Jang, Sung Kyu, et al. "Synthesis and characterization of hexagonal boron nitride as a gate dielectric." *Scientific reports* 6 (2016): 30449.

[35] Tian, Hao, et al. "Growth Dynamics of Millimeter-Sized Single-Crystal Hexagonal Boron Nitride Monolayers on Secondary Recrystallized Ni (100) Substrates." *Advanced Materials Interfaces* (2019): 1901198.

[36] Xu, Yong-Nian, and W. Y. Ching. "Calculation of ground-state and optical properties of boron nitrides in the hexagonal, cubic, and wurtzite structures." *Physical review B* 44.15 (1991): 7787.

[37] Dorneles, L. S., et al. "The use of simmons' equation to quantify the insulating barrier parameters in

Al/AlO x/Al tunnel junctions." *Applied physics letters* 82.17 (2003): 2832-2834.

[38] Dorneles, L. S., et al. "The use of simmons' equation to quantify the insulating barrier parameters in Al/AlO x/Al tunnel junctions." *Applied physics letters* 82.17 (2003): 2832-2834.

[40] Wu, Ernest Y., and R-P. Vollertsen. "On the Weibull shape factor of intrinsic breakdown of dielectric films and its accurate experimental determination. Part I: theory, methodology, experimental techniques." *IEEE Transactions on Electron Devices* 49.12 (2002): 2131-2140.

[41] Schlitz, Ruth A., et al. "Weibull analysis of dielectric breakdown in a self-assembled nanodielectric for organic transistors." *The Journal of Physical Chemistry Letters* 1.22 (2010): 3292-3297.

[42] Wu, Ernest Y., Baozhen Li, and James H. Stathis. "Modeling of time-dependent non-uniform dielectric breakdown using a clustering statistical approach." *Applied Physics Letters* 103.15 (2013): 152907.

Chapter 3. RRAM application of monolayer h-BN

3.1 Introduction and overview

3.1.1 Introduction of RRAM

RRAM and working principles

With the explosion in data generation and processing, the demand for improved storage memory devices is urgent. Resistive random-access memory (RRAM or ReRAM) is gaining tractions again recently as the next generation nonvolatile memories to replace traditional flash memories. Compared to the conventional memories, RRAM has a lot of advantages such as high stability, high speed, high-density capabilities, low power consumption, nonvolatility, and excellent compatibility with traditional CMOS technology [1-3].

General RRAM device configurations are capacitor-like meta-insulator-metal (MIM) "sandwich" structures. The basic working principle of RRAM is based on the reversible conversion property between high resistance state (HRS) and low resistance state (LRS) of the dielectrics. This change of resistance can be measured and read as a 1 or a 0. When resistance of the device switches from HRS to LRS, the process is defined as “set”, and inversely, the process from LRS to HRS is called “reset”. Normally, pristine devices start in a HRS and are put into LRS by applying a high voltage stress via soft dielectric breakdown (SBD), which is the forming process. For most films, especially exfoliated thin films, a forming process is indispensable. Then, set and reset processes can be operated to achieve the resistive switching (RS) performance. During the set process, the current is normally limited by the compliance current (CC) of the control system to avoid catastrophic hard breakdown (HBD).

On the basis of I–V characteristics, the resistive switching characteristics are classified into two types: nonvolatile resistive switching, involving bipolar resistive switching (BRS) and unipolar resistive switching (URS) behaviors, and volatile threshold (TH) switching. The devices showing BRS and URS behaviors can remain two stable states without applied bias. Therefore, they can undoubtedly be used as memories for non-volatile data storage, which means that the devices can hold saved data even when the power is turned off. And those devices revealing TH behaviors are not suitable for non-volatile memory applications because TH only shows one stable state when external stress is released. However, there are still many potential applications using TH, including electrical switches[4], smart windows[5], terahertz nano antennas [6], memory metamaterials[7], and selectors in a RRAM crossbar array[4, 8] which can solve a sneak path problem.

Resistive Switching Mechanisms

To date, massive experimental and theoretical studies on the resistive switching phenomenon have been carried out but an accurate resistance switching mechanism has not been determined. The proposed models can be grouped into different categories depending on the conducting path, driving force and switching behaviors.

In terms of the conductive paths model, conduction filament (CF) theory [9,10] and interface path model [11] were proposed. The CF theory is most accepted and is confirmed applicable in monolayer h-BN by the reversible dielectric breakdown study in Chapter 2. That is, the formation of percolation paths in the dielectrics leads to the forming and set process which turns the HRS to LRS, and the rupture of paths result

in the reset of devices. Meanwhile, some studies claim that the change of resistance is determined by the change in contact resistance of the interface between metal and the dielectrics.

By applying voltage on the MIM device, two main forces: electric field and Joule heat [12] are generated, which allow ions and electrons and heat transport, migrate and conduct among the devices. Therefore, the resistive mechanisms can also be classified into three types: ion effect, electronic effect and thermal effect. What needs to be mentioned is that these three effects are not completely isolated and independent. Instead, they may work together on a single device. Thus, specific mechanism determination requires detailed analysis of the electrical characteristics.

Of these three, the ion effect is the most commonly recognized mechanism of the current memristor. RS is caused by ionic motion and chemical redox reaction of ions as a result of electric field stress, and can be divided into cationic effect [13] and anion effect [14]. The cation effect is caused by electrochemically active metal electrode ion, such as Ag^{+}. Cu^{2+}, Ni^{+}, etc. The anion reactions are generally caused by ions of dielectric material, which are oxygen ions for metal oxide dielectrics, likewise boron ions for h-BN. Generally, polarity dependent ion reactions are responsible for the BRS mechanism. Unlike the ion migration chemical mechanism, electronic effects are completely based on the physical behavior of electrons. Several kinds of mechanisms have been proposed to explain the resistance change between HRS and LRS, including the trap charging and discharging, Ohmic conduction, Schottky emission, Pool–Frenkel (P–F) emission, and space charge limited current (SCLC), etc.[15]. Apart from the electric effect, the thermal effect can also influence the resistive switching processes, which is called Thermochemical Mechanism (TCM) [16]. Based on

conductive filament theory, the set process is regarded as an electric field driven filament formation event. In the reset process, abundant joule heat generated from CF provides energy, increasing the amplitude of atomic oscillation, so that the atom has a greater possibility of escaping from the CF, causing the rupture behavior. TCM is commonly regarded involving both metal and intrinsic dielectric defects contribution and usually attributed to the polarity independent events: URS and TH switching.

Bipolar Resistive Switching with self-compliance current

Unlike most cases of RS setting that require external current compliance to prevent hard breakdown of the dielectrics, there is one BRS phenomenon that can be achieved with a self-compliance current. This event can significantly reduce the power assumption of devices and is crucial for future high-density resistive switching memories. Normally, the self-compliance phenomenon is caused by the existence of internal resistance of the interface in a series with the RRAM resistance, where the interface is generally unintentionally induced and plays the role of current limiter [17]. The mechanism of switching can be explained based on carrier transport between the interface and dielectrics.

Conversion between Resistive Switching types

It is worth noting that nonvolatile BRS, URS effects and volatile TH phenomena are not strictly defined in certain MIM devices. Sometimes single device is able to show both a bipolar and unipolar switching modes, or both memory and TH events. The conversion between memory and TH can be achieved with some methods: by controlling the compliance current [18], by changing the ambient temperature[19], by modulating the film stoichiometry [18], and by varying the thickness of the electrode[20].The method

controlling the conversion between BRS and URS from literature is by adjusting the electrical power. Enlarging either the magnitude of compliance current [21, 22] or switching bias range [22] can switch BRS to URS, vice versa.

The coexistence and conversion of different switching types indicate that the basic mechanisms of these modes are associated. Therefore, a deeper study of the conversion mechanism is advantageous to a better understanding of the switching phenomena in RRAM devices. The coexistence of nonvolatile RS and volatile switching phenomena opens the potential that one device applied both as a memristor and a switch in the same arrays.

3.1.2 Overview

So far, metal oxides are the most widely investigation materials in the RRAM technology. The investigation of 2D insulating materials is still at early stage, with many problems remaining. As for the resistive switching study of h-BN film, the reported investigation regularly focused on multilayer film and non-volatile characteristics [23-27]. Nevertheless, the BRS with self-compliance current and the connection between different switch modes of h-BN has never been discussed yet.

Here, we concentrate on the evaluation of the RRAM device and the connection between different switching modes in monolayer h-BN. For this particular film, non-volatile BRS, URS and volatile TH switching phenomena are found to independently exist in distinct devices of the same sample. Then the standard memory performances of the BRS including the on/off ratio, retention, endurance, and reliability are characterized. Surprisingly, more than two switching modes are discovered to coexist in one device and

can be converted from one to the other by controlling the electrical power, the mechanisms behind are discussed in the end. Moreover, the influence of electrodes on the self-current compliant BRS behavior and the symmetry property of monolayer h-BN are also studied.

3.2 H-BN sample growth condition and nanoscale characterization

As in the previous project, we fabricate MIM devices from three MBE-grown monolayer h-BN films with bottom electrodes Ni or Co to investigate the RRAM performance. The growth conditions are summarized in Table 3.1, and corresponding structural and optical characterization results of Sample 2 and Sample 3 are shown in Figure 3.1 and 3.2, respectively. Sample 1 is the exact Sample 1 in Chapter 2, and the characterization is shown in Figure 2.3 of Chapter 2.2. Note that the h-BN of Sample 3 has graphite underneath which is also synthesized by MBE instead of directly growing on metal substrate like Sample 1 and 2.

Step	Parameters	Sample 1	Sample 2	Sample 3
Hydrogen Annealing	Substrate	Ni	Ni	Co
	Substrate temperature [ºC]	927	927	930
	Hydrogen gas flow [sccm]	10	10	10
	Duration [mins]	15	15	15
Carburization	Acetylene gas flow [sccm]	0.5	0.5	0.5
	Duration [s]	300	300	240
	Substrate temperature [ºC]	927	927	930
H-BN Growth	Substrate temperature [ºC]	927	927	900
	Boron cell temperature [ºC]	1170	1170	1170
	Ammonia gas flow [sccm]	5	5	4
	Nitrogen gas flow [sccm]	10	10	8
	Nitrogen ECR current [mA]	60	60	60
	Duration [hours]	7	7	6

Table 3.1. Summary of growth conditions of h-BN samples

Figure 3.1 summarizes the characterization results of Sample 2. Figure 3.1a shows an SEM image of the film. H-BN and Ni substrate appear relatively dark triangle flakes and bright area, respectively. Figure 3.1b shows a Raman spectrum of the transferred Sample 2. A characteristic E_{2g} phonon peak is found at 1370 cm^{-1}, implying that the film is a single layer [28]. Figure 3.1c shows an absorption spectrum of the transferred Sample on a sapphire substrate. A peak at 202 nm with a sharp absorption edge is observed. The inset shows its Tauc plot assuming a direct semiconductor. A bandgap of 6.0 eV is determined, which matches that of h-BN [29]. Figure 3.1d shows an AFM image of the transferred sample. The inset is a scanning profile across an edge of the transferred film, indicating a thickness of ~0.6 nm. With a consideration of AFM tip effect, this thickness suggests that the film is a monolayer [30].

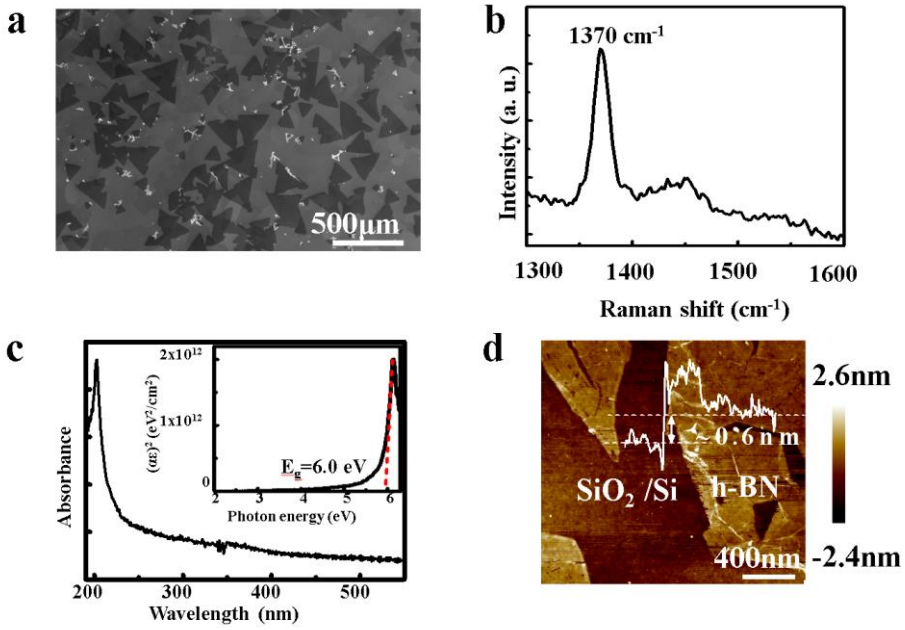

Figure 3.1 Characterization of 2D h-BN layer (Sample 2). (a) SEM image of h-BN film on Ni substrate. (b) Raman spectrum measured on the transferred h-BN on SiO_2/Si. (c) UV absorption spectrum of h-BN transferred onto a sapphire substrate. Inset shows the Tauc plot determining the optical bandgap. (d) AFM image scanning across the sample edge on the transferred h-BN on SiO_2/Si.

Figure 3.2 (a) shows the center region of as grown h-BN/G sample on Co substrate (Sample 3), which exhibiting continuous and uniform high-quality film. Figure 3.2 (b) shows Raman spectrum of an as-grown h-BN/G sample. The existence of both h-BN and multilayer Graphene (MG or thin Graphite) Raman peaks is evident. The spectrum indicates the E_{2g} phonon mode's position of h-BN at ~1367 cm^{-1} with full width at half maximum FWHM at ~65 cm^{-1}, and the 2D/G intensity ratio of MG in this sample is calculated ~0.35. Figure 3.2 (c) is an absorption spectrum of the sample after a portion of the h-BN/MG film was transferred to a sapphire substrate. The clear absorption edge at ~202 nm originates from the band gap of h-BN film [29]. A big portion of UV light spectrum has been also absorbed by the thick MG film [31]. The inset is the Tauc plot determining the optical bandgap around 5.5 eV. A portion of the sample was transferred onto SiO_2/Si substrate for the AFM measurement. The AFM image reveals that the h-BN/G film has a total thickness of ~133 nm (Figure 3.2 (d)). To reveal the individual thickness of h-BN and MG layers, we performed XPS sputtering depth profile measurement. Figures 3.2(e) and (f) show the evolution of C1s, and B1s and N1s XPS signals as a function of sputtering depth within 4 nm of the top surface of h-BN/G sample at 284.6 eV, 190.4 eV, and 397.9 eV, respectively. As seen in Figure 3.2 (e), C1s peak is strongest when the sample was not sputtered, which is due to the inclusion of signals from absorbed C species on the surface or adventitious C [32]. After removing the top 0.17 nm material, the intensity of C1s peak drops significantly compared with the signal before sputtering and then remains about the same with further sputtering while the width of the C1s peak increases as the sputtering depth increases due to Ar^+ beam induced damage. On the other hand, B1s and N1s XPS signals in Figure 3.2(f) decrease proportionally and gradually by removing the

top layers and become negligible when the sputtering depth reaches ~0.5 nm (i.e., h-BN thickness). It can be concluded that the h-BN/MG structure has a top h-BN layer of 0.5 nm and a bottom MG layer of 132 nm. We believe that the h-BN is most likely monolayer, in contrast to 1-2nm as suggested in the previous report [33].

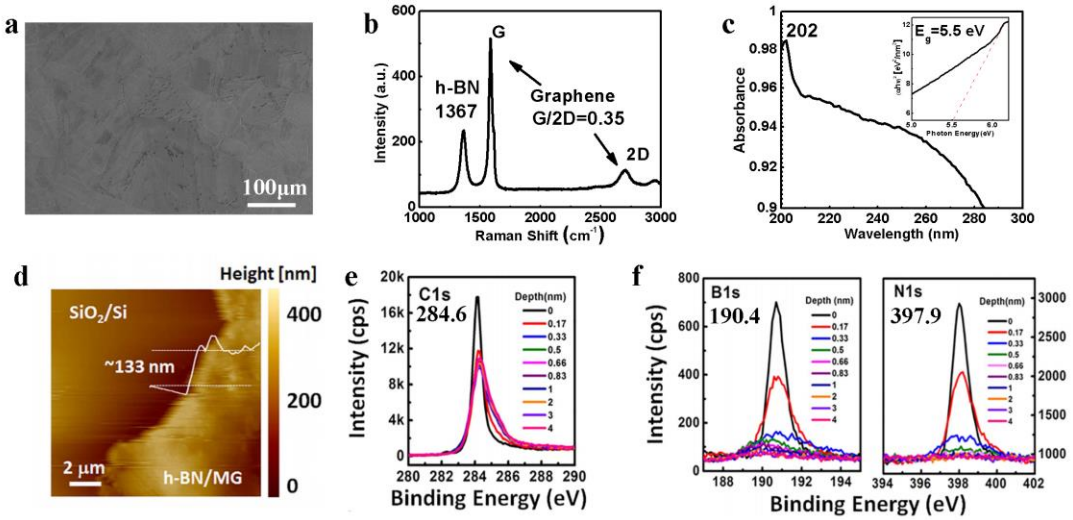

Figure 3.2 Characterization of h-BN/Gr sample (Sample 3). (a) SEM image of continuous h-BN/Gr film on Co substrate. (b)Raman spectrum measured directly on the h-BN/Gr on Co. (c) UV absorption spectrum of h-BN transferred onto a sapphire substrate. Inset shows the Tauc plot determining the optical bandgap. (d) AFM image of the same sample transferred onto SiO_2/Si substrate with the total thickness of ~133 nm. (e) C1s and (f) B1s and N1s as a function of sputtering depth in the depth-profile XPS characterization.

3.3 Resistive switching behaviors

3.3.1 Bipolar, unipolar and threshold switching modes

In the monolayer h-BN based MIM devices, we observed the existence of the three types of RS, namely, BRS, URS and TH from different devices on the same sample. Therefore, we can describe the basic features of I–V curves for each type of RS phenomena as shown in Figure 3.3, which reveal the three forming free switching modes from three distinct Au-h-BN-Ni devices of Sample 1.

This forming-free process can avoid unpredictable resistance states resulted from relative higher bias and compliance current value operation. The intrinsic defects like abundant boron vacancy clusters or metallic ions are mostly likely the attribution of the electroforming-free behavior according to the previous claim in metal oxides [33,34].

The first step of switching from HRS to LRS in each behavior is identical, which is trigged by applying external voltage stress until SBD event. This process is denoted as “set” in BRS and URS, and called “Turn on” in TH switching. However, the operations from LRS to HRS of the three behaviors are totally different from each other. BRS requires both polarities of voltage to achieve the resistance switching, namely, the “reset” process from LRS to HRS occurs at the reverse voltage polarity of the set voltage. Normally, the I-V characteristic of BRS is asymmetric with respect to polarity. When the set occurs at the positive polarity and reset takes place at the negative polarity, the BRS is called figure-of-eight (F8), just like Figure 3.3 (a) shows. On the other hand, when the set is initialized at the negative polarity and reset happens at the positive polarity, the BRS is referred as counter-figure-eight (cF8). Whereas, URS depends on the amplitude of the external voltage rather than on the polarity. By applying voltage with the same polarity and direction of voltage to the set stress, the device can “reset” from LRS back to HRS abruptly once voltage reaches V_{reset}, which is normally smaller than V_{set} as shown in Figure 3.3 (b). The revert from LRS to HRS of TH behavior is named “Turn off”, which takes place while voltage is sweeping back with the same polarity but smaller value than the “Turn on” process.

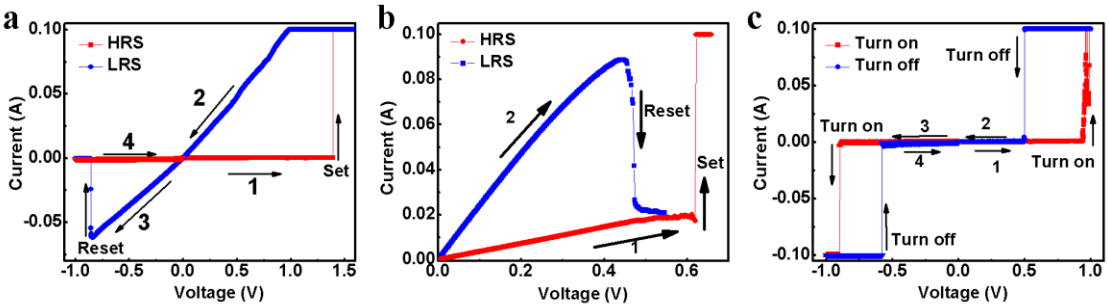

Figure 3.3 I-V characteristics on three distinct Au-h-BN-Ni devices showing forming free (a) non-volatile BRS mode, (b) non-volatile URS mode, and (c) volatile threshold (TH) switching mode. The compliance current is 100mA.

3.3.2 Memory performance

Figure 3.4 shows characterization results of the BRS behaviors on a device with Au- h-BN-Ni configuration from Sample 2. Figure 3.4 (a) exhibits good endurance with 97 cF8 BRS DC cycles at 100mA CC at room temperature. Figure 3.4 (b) demonstrates the retention property of the HRS and LRS by measuring the current at constant bias 0.1V. The HRS retention remains stable, but the LRS exhibits self-recovering property to HRS when time exceeds several hundred seconds. The reliability is an issue because the On/Off ratio (R_{high}/ R_{low}) varies from 10^1 to 10^4 with a 10^3 average window as Figure 3.4 (c) shows. The high variability is caused by the high variability of HRS, which is related to the configuration of CF. On the other hand, the set and reset voltage variability is quite low as Figure 3.4 (d) shows with average voltages: V_{set} =-0.87V and V_{reset} =0.70V.

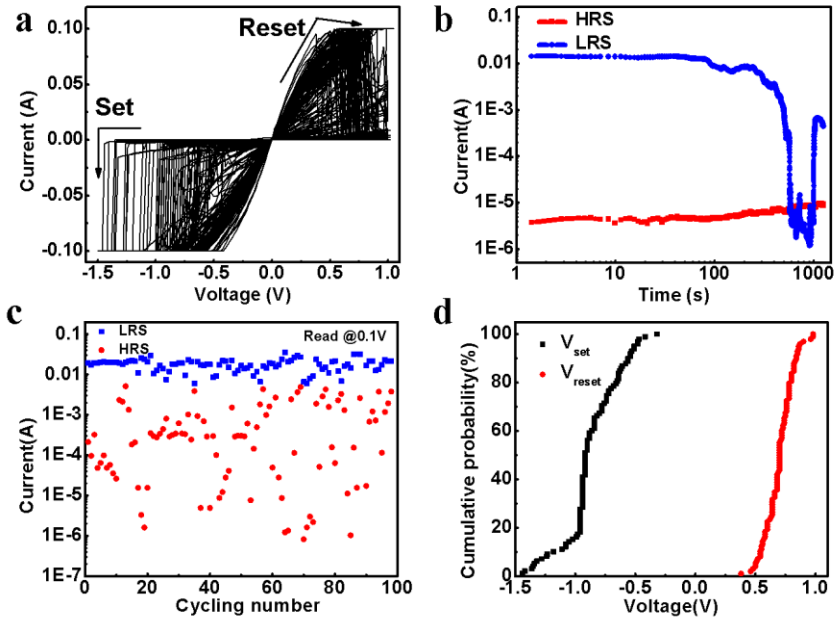

Figure 3.4 BRS performance on an Au-h-BN-Ni device with size 50x50 μm^2 from Sample 2. (a) I-V characteristics of successive 97 BRS cycles; (b) Time dependent current measurements featuring stable LRS but unsatisfied HRS retention at room temperature. The current of the HRS and LRS is measured at the bias of 0.1 V; (c) The dispersion of both HRS and LRS in terms of the current read at 0.1V with the 97 cycles; (d) The cumulative set and reset voltage distribution.

3.3.3 Self- current compliant BRS and conversion of different switching modes

The conversion between different switching modes in one device can be grouped into two types: the conversion between BRS and URS, and the conversion between memory and TH switching. Interestingly, in monolayer h-BN based MIM devices, both events are found. In addition, accompanying the conversion in the structure with Graphite bottom electrode, the BRS with self-compliant current event of h-BN is also discovered for the first time. In our experiment, the switching conversion always starts from BRS regardless of the current magnitude. The method of controlling the conversion from BRS to other switching mode is by increasing the electrical power, either by enlarging the applied voltage (Figure 3.5) or by increasing the compliance current value (Figure 3.6).

Figure 3.5 shows the conversion from (a) BRS modes to (b)TH and (c) URS in sequence at same CC value on a Pt-h-BN-Ni device. The set voltage of both the converted TH and URS is larger than that of the initial BRS. Note that the only parameter determining the converted mode of TH or URS is the voltage sweep direction operation. Thus, the mechanism of conversion from BRS to URS or to nonvolatile TH should be identical.

Figure 3.6 exhibits the reversible conversion of self-current compliant BRS and URS with higher compliance current on one Au-h-BN-Graphite-Co device. Figure 3.6 (a)-(d) shows the process starting from the BRS with a self-compliant current of 0.4 mA to URS by increasing the compliance current to 10mA, then resets back to BRS with self-limited current 0.4 mA and ends up with URS with high compliance current 50mA in sequence.

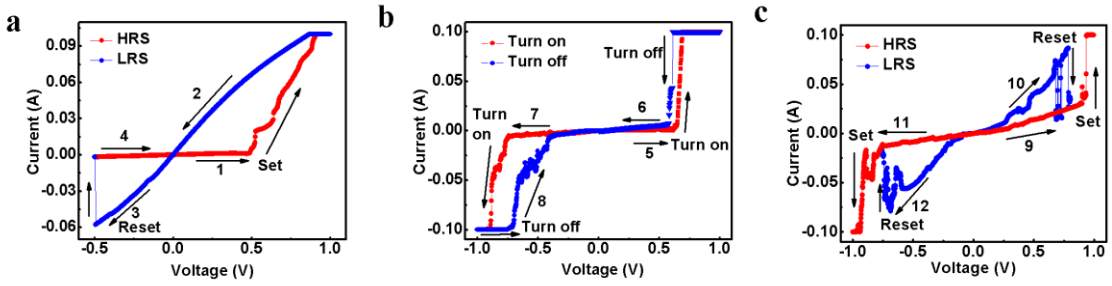

Figure 3.5 I-V characteristics in sequence on one Pt-h-BN-Ni device, (a)-(c) shows the conversion from BRS to TH switching, and URS with respect to the increase of the set voltage.

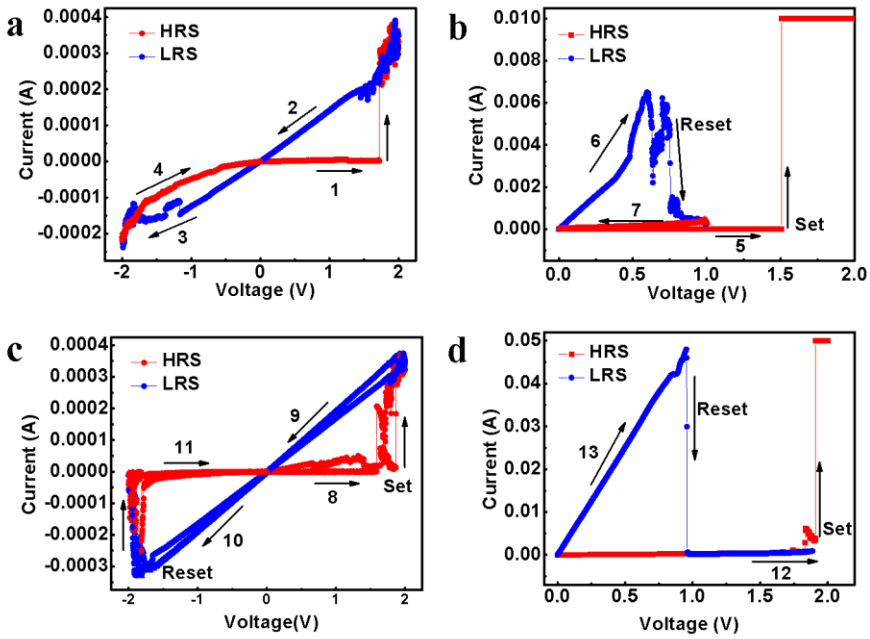

Figure 3.6 I-V characteristics in sequence on one Au-h-BN-Graphite-Co device, (a)-(d) shows the conversion from BRS with self-compliance current to URS, and resets back to BRS, and move on to URS behavior in sequence. Conversion of BRS and URS is controlled by compliance current value.

3.3.4 The influence of electrodes on RS phenomena

In order to figure out the mechanisms of the switching, we deposited multiple electrodes including inert electrode Pt, Au and active electrode Ni and Co on as grown h-BN samples. There were five configurations utilized: Ni-h-BN-Ni, Pt-h-BN-Ni, Au-h-BN-Ni, Co-h-BN-Gr-Co, and Au-h-BN-Gr-Co. The standard RS properties studied include the forming free necessity, the electrical symmetric characterization, the individual existence of BRS, URS and TH, the appearance of BRS with self-compliant current and the coexistence and conversion between different switching modes.

Besides the I-V characteristics of the RS behaviors from 3.1-3.3, the complementary RS phenomena with different configuration are illustrated in Figure 3.7. All the above RS phenomena is summarized in Table 3.2. In Figure 3.7, every three figures on the same row reveal the characteristics of the same structure. Figure

3.7 (a)-(c) are collected on Ni-h-BN-Ni, (a)-(b) demonstrates the conversion from BRS to URS on one device at the same CC 100mA, and (c) exhibits an individual TH behavior of another device on this structure. Figure 3.7 (d)-(f) show independent BRS, URS and TH events on distinct Pt-h-BN-Ni devices. Figure 3.7 (g)-(i) are collected on Co-h-BN-Gr-Co structure, (g) and (h) demonstrate the transition from the BRS with self-compliance current 0.2 mA to URS by increasing the cc to 10 mA as well as the voltage stress, and (i) is an example of independent TH characteristics with 50 mA cc. Figure 3.7 (j)-(l) show the individual BRS, URS and TH behaviors on Au-h-BN-Gr-Co with a cc100 mA, which proves that the appearance of all RS behaviors at all compliance currents.

Device structure	**Forming process**	**BRS**	**URS**	**TH**	**Conversion**	**Self-CC-BRS**
Ni-h-BN-Ni Pt-h-BN-Ni Au-h-BN-Ni	No	Yes	Yes	Yes	Yes	No
Co-h-BN-Gr-Co Au-h-BN-Gr-Co	No	Yes	Yes	Yes	Yes	Yes

Table 3.2 RS Phenomena summary on monolayer h-BN film with various electrodes.

Overall, all the structures exhibit forming-free independent URS, BRS and TH phenomena in distinct devices and the conversion between different modes by modulating the electrical power. It is found that irrespective of symmetric or asymmetric configurations, both F8 BRS and cF8 BRS can coexist. The difference caused by the electrode on the RS performance is that the BRS with self- compliant current event is only found on the devices with graphite bottom electrode.

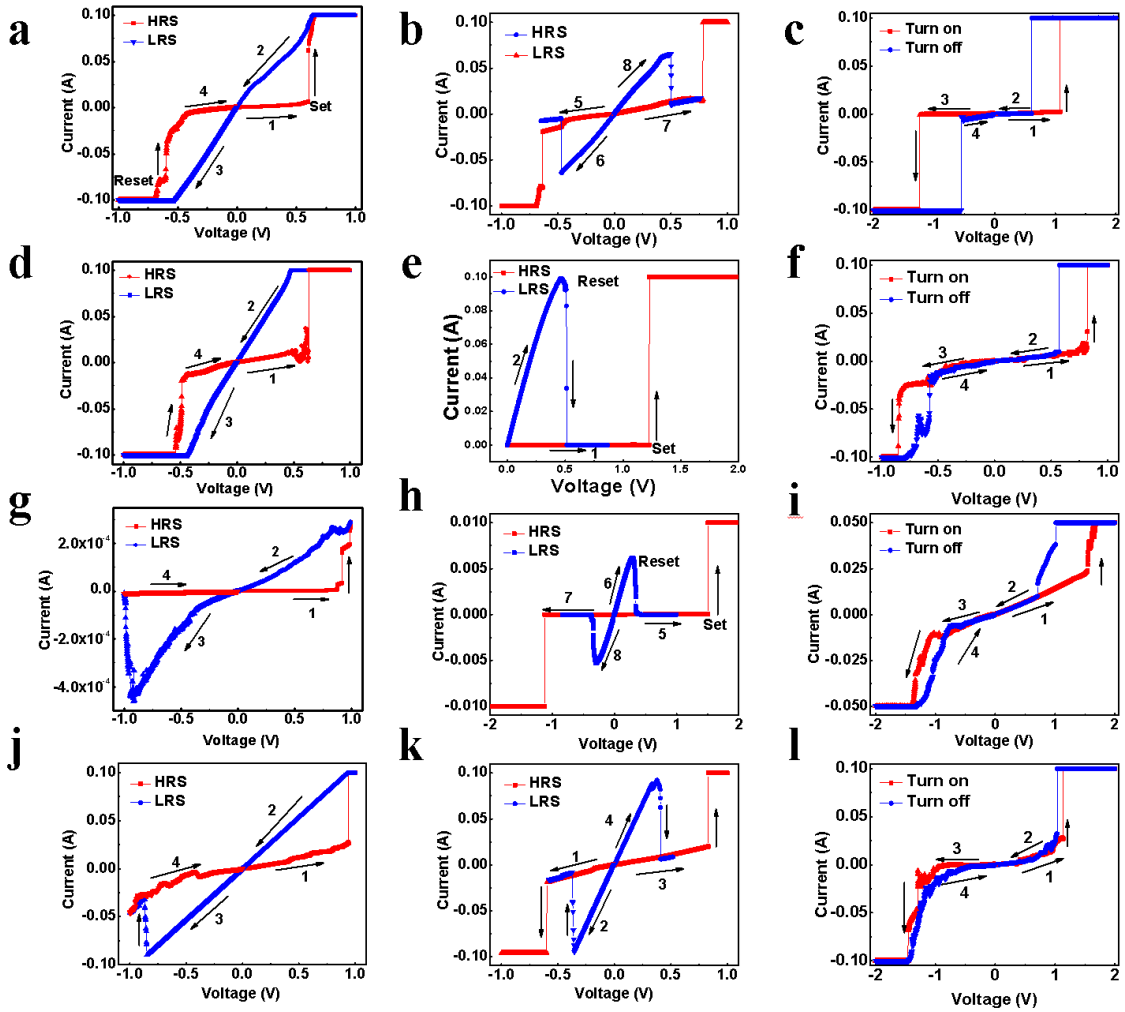

Figure 3.7 RS Phenomena summary on monolayer h-BN film with various electrodes. (a)-(c) are collected from Ni-h-BN-Ni, (a)-(b) BRS conversion to URS on one device, (c) individual TH behavior; (d)-(f) show independent BRS, URS and TH events on are on Pt-h-BN-Ni.(g)-(i) are collected on Co-h-BN-Gr-Co; (g) and (h) demonstrate the transition from BRS with self-compliant current to URS; (i) is an example of independent TH characteristics; (j)-(l) show the independent BRS, URS and TH behaviors on Au-h-BN-Gr-Co with a cc 100 mA.

3.4 Mechanism discussion

The previous RS properties of monolayer h-BN are quite interesting but also very intriguing. In this section, we will analyze the mechanisms behind by referring reported models in similar devices.

The conductive channels of monolayer h-BN have been proven following percolating CFs through electrodes in chapter 2. The development of CFs by electric force gives rise to the set process, and the rupture of CFs leads to the reset step. As we know, the films grown by epitaxy methods unavoidably contain intrinsic defects, in our case, boron vacancies, Ni or Co ions, etc. These defects play a key role in the resistive switching performance. The forming- free process was proven promoted by the grain boundaries. BRS behaviors are attributed to the polarity-dependent physical process, which are the reactions and transportations of defects, including the redox and movement of metal and boron ions, and electrons trap and de-trap, etc. The reset process of URS and TH behaviors is ascribed to the escaping of defects from CFs driven by Joule heat. The collective activities of electronic effect, ion effect and thermal effect contribute to the RS of monolayer h-BN.

Besides the general description of RS model, the investigation of conversion between different switching modes is crucial to the understanding of unified mechanisms. We will discuss the models of conversion from BRS to URS or TH at the same cc as well as the conversion from BRS with self-compliant current.

The conversion between BRS, URS and TH under the same compliance current

Normally, studies discuss the conversion of BRS and URS and the conversion between memory and TH

separately because the CF configurations of two conversions are considered different. The CFs created in URS and TH are regarded identical as the complete CF connecting two electrodes but whether CF formed in BRS is a complete CF is still controversial. In our case, since the three switching modes are able to convert to each other under the same cc and close voltage sweep range, their percolation natures are supposed to be similar. The transformation from BRS to the other two modes is most likely due to the conversion of dominant driving force and the thermal stability of CF. These two models were supported by experiments between BRS and URS and a temperature cycling experiment on the conversion between BRS and TH switching [36], respectively. We believe these two models are related to work in the conversion. Figure 3.8 is the schematic diagram of the conversion process.

At the beginning of the device operation, which is at low ambient temperature, a stable CF is able to form in the set process. The CF is stable at low temperature and turns unstable at high temperature. Under this circumstance, electric force dominates the RS and promotes the polarity dependent ionic motions, resulting in the BRS.

With the accumulation of the RS cycles, the surrounding temperature is sufficiently high. Then the CF developed during the set process is relatively unstable and Joule heat is stronger than the electric field energy, which makes polarity independent URS and TH easier created.

When the heat is dissipated and CF is ruptured in the reset process of URS or TH, the device can recover to pristine state. That's why the switching mode can be turned back to BRS again. But in most cases, Joule heat keeps as the dominant driving force over electric force in the later stage of the conversions due to the

insufficient thermal dissipation, which develops TH and/or URS more frequently.

The conversion between BRS with self-compliant current and URS

It is widely accepted that the CFs in BRS with self-compliant current is incomplete percolating channels between the electrodes. There is a current limiter providing the internal resistance in series with the incomplete CF during the set process. The current limiter is normally unintentionally induced defects or intentionally inserted metal oxides between the insulator and one side of electrode.

The exclusive occurrence of self-current compliant BRS on devices with Graphite bottom electrodes indicates that the interface between h-BN and Graphite works as the current limiter, which is in series with the incomplete CF penetrating h-BN and top electrode. The gap between the CF and Graphite electrode keeps insulating or semiconducting during the self-current compliant BRS process owing to some unknown defects. When a dramatically enhanced compliance current is applied, a fully percolating CF through two electrodes is successfully generated by the aggregation of boron ions or electrons in the gap between Graphite and h-BN, which belongs to the set process of URS. Then the thermal annealing process due to Joule heating locally ruptures the fully CF between two electrodes, the device is reseted to original state, allowing the conversion between two modes repeat. This procedure is summarized in Figure 3.9.

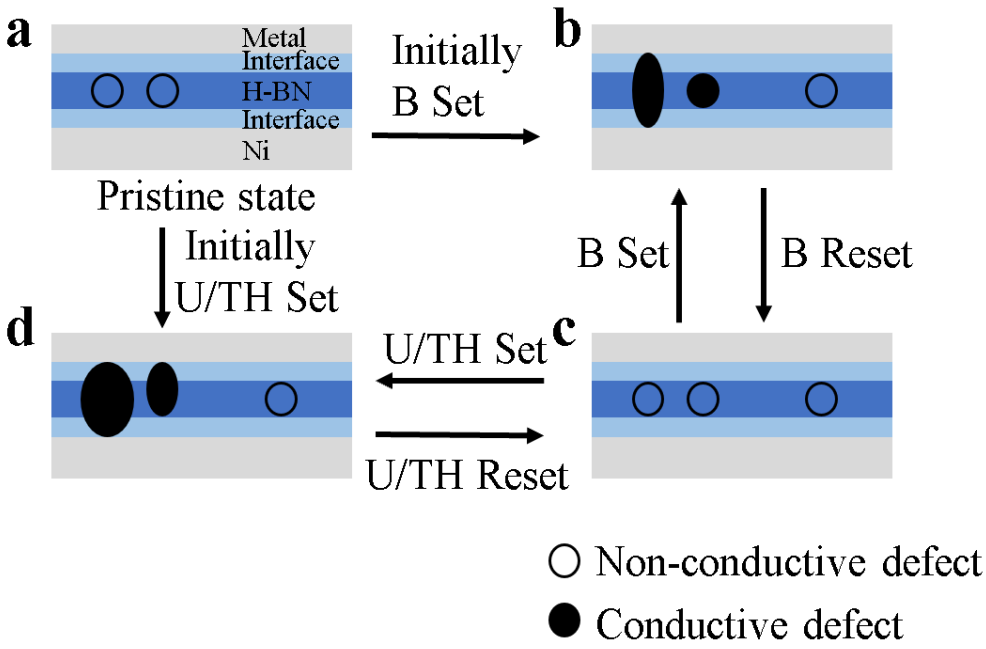

Figure 3.8 Schematic diagram of the resistive switching mechanisms of Metal-h-BN-Ni devices. The top electrodes in our experiments include Ni, Au and Pt. (a) Pristine state. Silver, dark blue and light blue areas represent the electrodes, h-BN and interfaces, respectively. Hollow circles are non-conductive defects. The percolating path denoted by a solid black path in (b) and (d) connecting the two terminal electrodes through monolayer h-BN and the interface between h-BN and electrodes. The initial developed conduction filaments are normally very stable like (b) shows, and the LRS of BRS operation can be achieved with respect of bias. By applying the opposite voltage, the CF ruptures so that the devices are able to recover to the HRS shown in (c). If the CF are less stable compared to (b), as shown in (d), which is either formed from the initial state or followed BRS events by increasing the electric power. Then, Joule heat dominates the driving force of the resistive switching, indicating the reversible URS or TH mode can be obtained depending on the following external bias sweep direction.

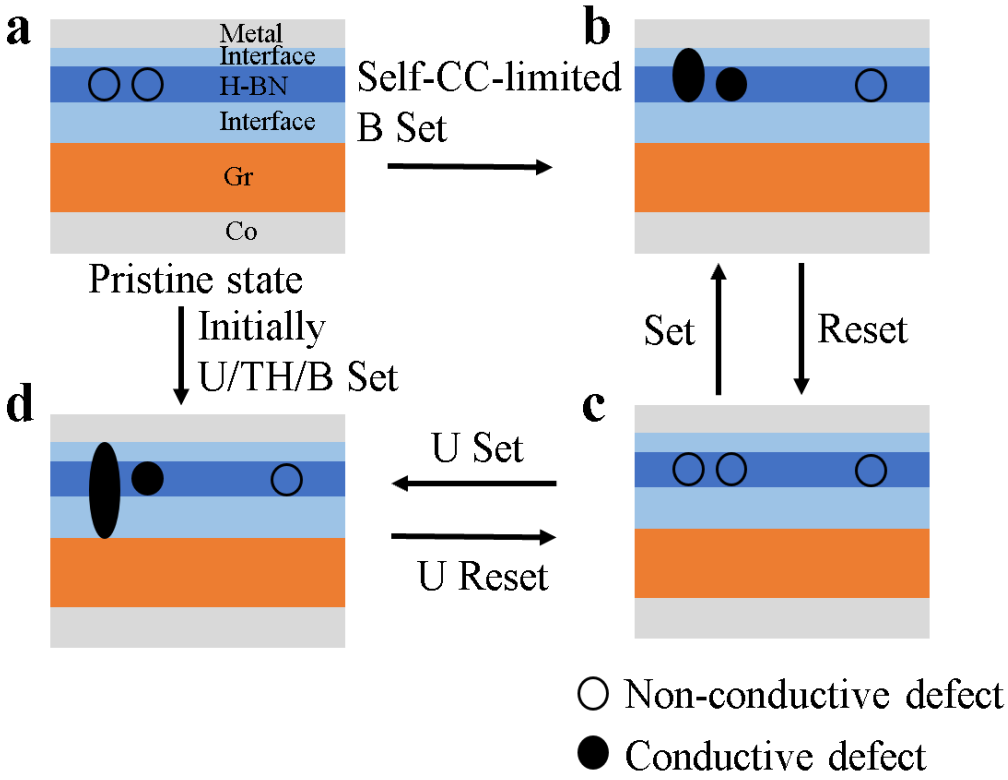

Figure 3.9 Schematic diagram of the resistive switching mechanisms of Metal-h-BN-Gr-Co devices, Au and Co are used as top electrodes. Silver, dark blue, light blue and brown areas represent the electrodes, h-BN, interfaces and Graphite, respectively. Hollow circles and solid dots are non-conductive and conductive defects, respectively. (a) Original state. (b) When an incomplete CF is formed, the LRS of self compliance current limited BRS is initialized. The current limiter is most probably emerged in the interface between h-BN and Graphite. (c) The break of the incomplete CF turns the device back to HRS. If the electric power is enhanced after (c) or large enough initially after (a), then the complete CF between the two electrodes is able to be formed. And BRS, URS and TH with compliance current can be achieved depending on the polarity and direction of the later bias.

3.5 Conclusion and future working direction

In this work we investigate the presence and the mechanism of RS in monolayer h-BN film using MIM configurations. It is found that irrespective of whether electrode is active or inert, symmetric or asymmetric, all of the devices display polarity independent RS behaviors. All the MIM devices of monolayer h-BN show independently existence of forming-free nonvolatile BRS, URS and volatile TH behaviors. In

terms of the memory characteristics, BRS performance exhibits good endurance with 97 cycles at 100mA CC, an average on/off window of 10^3 , low set and reset voltage variability, but unsatisfied retention. The only influence of electrode on the performance is that the devices with Graphite electrode demonstrate self-compliant current BRS and corresponding reversible current dependent conversion from BRS to URS modes compared to those with both metal electrodes, which is the first time discovered from h-BN as well as atomic sheet, makeing monolayer h-BN useful for low power applications. The conversions between different switching modes are controlled by electrical power, either by compliance current magnitude or voltage bias sweep range.

The formation and rupture of CFs are responsible for the set and reset process. The set process is indeed SBD, which is driven by electric field to activate intrinsic defects like grain boundaries in h-BN, as they allow easy B vacancies generation, metallic ion penetration and electron trapping so as to create conductive paths. The reset process ruptures the conductive paths by either electric field which normally behaves as BRS or thermal dissipation that displays URS and TH switching. The conversion from BRS to URS and/or TH at same cc is due to the change of driving force and the thermal stability of CFs. The conversion from BRS with self-compliance current to URS with high current is the conversion of CF configuration, where the interface between h-BN and Graphene works as the current limiter in self-limited BRS.

However, some problems remain to be solved to improve the memory performance and toward potential application. The most significant issue to get better BRS characteristics is to obtain reliable HRS,

which requires controllable thermal dissipation in the Reset process of DC stress. Besides material properties, the operation of device also indirectly influences electrical parameters. Therefore, several optimized operation schemes like optimized operation schemes in pulse voltage operation and current stress mode to replace conventional DC voltage stress and voltage stress mode are also worth carried out. In addition, it is very important to get controllable and repeatable self- current compliant BRS in terms of low power consumption. In order to work as a selection device in high density cross-point type structures for RRAM, the TH characteristics requires thermal stability, uniform switching behavior, high endurance, and high switching speeds, which are all needed to be tested in the future. Last but not least, further mechanism confirmation relies on nanoscale characterization like C-AFM, cross-sectional TEM, SEM, etc.

3.6 References

[1] Dearnaley, G., A. M. Stoneham, and D. V. Morgan. "Electrical phenomena in amorphous oxide films." *Reports on Progress in Physics* 33.3 (1970): 1129.

[2] Lee, Jae Sung, Shinbuhm Lee, and Tae Won Noh. "Resistive switching phenomena: A review of statistical physics approaches." *Applied Physics Reviews* 2.3 (2015): 031303.

[3]. Li Y, Long S, Liu Q, et al. Resistive Switching Performance Improvement via Modulating Nanoscale Conductive Filament, Involving the Application of Two-Dimensional Layered Materials[J]. Small, 2017, 13(35):1604306.

[4] Chang, Seo Hyoung, et al. "Oxide double-layer nanocrossbar for ultrahigh-density bipolar resistive memory." *Advanced materials* 23.35 (2011): 4063-4067.

[5] Kato, Kazuhiro, et al. "Study on thermochromic VO2 films grown on ZnO-coated glass substrates for “smart windows”." *Japanese journal of applied physics* 42.10R (2003): 6523.

[6] Seo, Minah, et al. "Active terahertz nanoantennas based on VO2 phase transition." *Nano letters* 10.6 (2010): 2064-2068.

[7] Driscoll, Tom, et al. "Memory metamaterials." *Science* 325.5947 (2009): 1518-1521.

[8] Lee, M-J., et al. "Two series oxide resistors applicable to high speed and high density nonvolatile memory." *Advanced Materials* 19.22 (2007): 3919-3923.

[9] Chakrabarti, Bikas K., and Lucien-Gilles Benguigui. *Statistical physics of fracture and breakdown in disordered systems*. Vol. 55. Oxford University Press, 1997.

[10] Chae, Seung Chul, et al. "Random circuit breaker network model for unipolar resistance switching." *Advanced Materials* 20.6 (2008): 1154-1159.

[11] Sawa, Akihito. "Resistive switching in transition metal oxides." *Materials today* 11.6 (2008): 28-36.

[12] Yang, J. Joshua, Dmitri B. Strukov, and Duncan R. Stewart. "Memristive devices for computing." Nature nanotechnology8.1 (2013): 13.

[13] Valov, Ilia, et al. "Electrochemical metallization memories—fundamentals, applications, prospects." *Nanotechnology* 22.25 (2011): 254003.

[14]Waser, Rainer, and Masakazu Aono. "Nanoionics-based resistive switching memories." *Nanoscience And Technology: A Collection of Reviews from Nature Journals*. 2010. 158-165.

[15]Lim, Ee Wah, and Razali Ismail. "Conduction mechanism of valence change resistive switching memory: a survey." *Electronics* 4.3 (2015): 586-613.

[16] Wang, Zhongrui, et al. "Memristors with diffusive dynamics as synaptic emulators for neuromorphic computing." *Nature materials* 16.1 (2017): 101.

[17] Ye, Cong, et al. "Low-power bipolar resistive switching TiN/HfO2/ITO memory with self-compliance current phenomenon." *Applied Physics Express* 7.3 (2014): 034101.

[18] Peng, Hai Yang, et al. "Deterministic conversion between memory and threshold resistive switching via tuning the strong electron correlation." *Scientific reports* 2 (2012): 442.

[19] Chang, S. H., et al. "Occurrence of both unipolar memory and threshold resistance switching in a NiO film." *Physical review letters* 102.2 (2009): 026801.

[20] Chang, S. H., et al. "Effects of heat dissipation on unipolar resistance switching in Pt/ Ni O/ Pt capacitors." *Applied Physics Letters* 92.18 (2008): 183507.

[21] Jeong, Doo Seok, Herbert Schroeder, and Rainer Waser. "Coexistence of bipolar and unipolar resistive switching behaviors in a Pt/ TiO2/ Pt stack." *Electrochemical and solid-state letters* 10.8 (2007): G51-G53.

[22] Shen, Wan, Regina Dittmann, and Rainer Waser. "Reversible alternation between bipolar and unipolar resistive switching in polycrystalline barium strontium titanate thin films." *Journal of Applied Physics* 107.9 (2010): 094506.

[23]. Pan, Chengbin, et al. "Coexistence of grain-boundaries-assisted bipolar and threshold resistive switching in multilayer hexagonal boron nitride." *Advanced Functional Materials* 27.10 (2017): 1604811.

[24] Pan, Chengbin, et al. "Model for multi-filamentary conduction in graphene/hexagonal-boron-nitride/graphene based resistive switching devices." *2D Materials* 4.2 (2017): 025099.

[25] Qian, Kai, et al. "Hexagonal boron nitride thin film for flexible resistive memory applications." *Advanced Functional Materials* 26.13 (2016): 2176-2184.

[26] Ge, Ruijing, et al. "Towards Universal Non-Volatile Resistance Switching in Non-metallic Monolayer Atomic Sheets." *arXiv preprint arXiv:1709.04592* (2017).

[27] Chandni, U., et al. "Evidence for defect-mediated tunneling in hexagonal boron nitride-based junctions." *Nano letters* 15.11 (2015): 7329-7333.

[28] Arenal, Raul, et al. "Raman spectroscopy of single-wall boron nitride nanotubes." *Nano letters* 6.8 (2006): 1812-1816.

[29] Elias, Christine, et al. "Direct band-gap crossover in epitaxial monolayer boron nitride." *Nature communications* 10.1 (2019): 2639.

[30] Khan, Majharul Haque, et al. "Synthesis of large and few atomic layers of hexagonal boron nitride on melted copper." *Scientific reports* 5 (2015): 7743.

[31] Meng, Jun Hua, et al. "Synthesis of in-plane and stacked graphene/hexagonal boron nitride heterostructures by combining with ion beam sputtering deposition and chemical vapor deposition." *Nanoscale* 7.38 (2015): 16046-16053.

[32] Barr, Tery L., and Sudipta Seal. "Nature of the use of adventitious carbon as a binding energy standard." *Journal of Vacuum Science & Technology A: Vacuum, Surfaces, and Films* 13.3 (1995): 1239-1246.

[33] Khanaki, Alireza, et al. "Effect of high carbon incorporation in Co substrates on the epitaxy of hexagonal boron nitride/graphene heterostructures." *Nanotechnology* 29.3 (2017): 035602.

[34] Xu, Nuo, et al. "Characteristics and mechanism of conduction/set process in TiN/ ZnO/ Pt resistance switching random-access memories." *Applied Physics Letters* 92.23 (2008): 232112.

[35] Cao, Xun, et al. "Forming-free colossal resistive switching effect in rare-earth-oxide Gd_2O_3 films for memristor applications." *Journal of Applied Physics* 106.7 (2009): 073723.

[36] Chang, S. H., et al. "Occurrence of both unipolar memory and threshold resistance switching in a NiO film." *Physical review letters* 102.2 (2009): 026801.